PFG

Photogrammetrie Fernerkundung Geoinformation

Journal for Photogrammetry, Remote Sensing and Geoinformation Science

Organ der Deutschen Gesellschaft für Photogrammetrie, Fernerkundung und Geoinformation (DGPF) e. V.

Jahrgang 2015, Heft 5

E. Schweizerbart'sche Verlagsbuchhandlung
(Nägele u. Obermiller) Stuttgart 2015

Deutsche Gesellschaft für Photogrammetrie, Fernerkundung
und Geoinformation (DGPF) e.V.
Gegründet 1909

Die *Deutsche Gesellschaft für Photogrammetrie, Fernerkundung und Geoinformation* (DGPF) e.V. unterstützt als Mitglieds- bzw. Trägergesellschaft die folgenden Dachverbände:

International Society
for Photogrammetry
and Remote Sensing

Deutsche Arbeits-
gemeinschaft für
Mustererkennung e.V.

Herausgeber:

Präsident: Prof. Dr. Thomas Kolbe, Technische Universität München, Institut für Geodäsie, GIS und Landmanagement, Lehrstuhl für Geoinformatik, Arcisstraße 21, 80333 München, Germany, Tel. +49-89-289-23888
Geschäftsstelle: Tanja Nyc, c/o Technische Universität München, Institut für Geodäsie, GIS und Landmanagement, Lehrstuhl für Geoinformatik, Arcisstraße 21, 80333 München, Germany, Tel.: +49-89-289-22578, e-mail: geschaeftsstelle@dgpf.de
Published by: E. Schweizerbart'sche Verlagsbuchhandlung (Nägele u. Obermiller), Johannesstraße 3A, 70176 Stuttgart, Germany, Tel.: +49-711 351456-0, Fax: +49-711 351456-99, e-mail: mail@schweizerbart.de
Internet: http://www.schweizerbart.de
♾ Gedruckt auf alterungsbeständigem Papier nach ISO 9706-1994

ISSN 1432-8364 / e-ISSN 2363-7145
Science Citation Index Expanded (also known as SciSearch®) Journal Citation Reports/Science Edition
Hauptschriftleiter: Prof. Dr.-Ing. Wolfgang Kresse, Hochschule Neubrandenburg, Fachbereich Landschaftswissenschaften und Geomatik, Brodaer Straße 2, 17033 Neubrandenburg, Germany, e-mail: kresse@hs-nb.de
Schriftleiter: Prof. Dr.-Ing. Stefan Hinz, Karlsruher Institut für Technologie – KIT, Institut für Photogrammetrie und Fernerkundung, Englerstraße 7, 76131 Karlsruhe, Germany, e-mail: stefan.hinz@ipf.uni-karlsruhe.de, Prof. Dr. techn. Franz Rottensteiner, Leibniz Universität Hannover, Institut für Photogrammetrie und GeoInformation, Nienburger Straße 1, 30167 Hannover, Germany, e-mail: rottensteiner@ipi.uni-hannover.de, Prof. Dr. rer. nat. Christopher Conrad, Universität Würzburg, Institut für Geographie und Geologie, Oswald-Külpe-Weg 86, 97074 Würzburg, Germany, e-mail: christopher.conrad@uni-wuerzburg.de, Prof. Dr. rer. nat. Lars Bernard, Technische Universität Dresden, Fachrichtung Geowissenschaften, Helmholtzstraße 10, 01062 Dresden, Germany, e-mail: lars.bernard@tu-dresden.de, und Dr.-Ing. Eckhardt Seyfert, Landesvermessung und Geobasisinformation Brandenburg, Heinrich-Mann-Allee 103, 14473 Potsdam, Germany, e-mail: eckhardt.seyfert@geobasis-bb.de
Erscheinungsweise: 6 Hefte pro Jahrgang.
Bezugspreis im Abonnement: € 249,– pro Jahrgang. Mitglieder der DGPF erhalten die Zeitschrift kostenlos. Der Online-Zugang ist im regulären Subskriptionspreis enthalten.
Anzeigenverwaltung: E. Schweizerbart'sche Verlagsbuchhandlung (Nägele u. Obermiller), Johannesstraße 3A, 70176 Stuttgart, Germany, Tel.: +49-711 351456-0; Fax: +49-711 351456-99.
e-mail: mail@schweizerbart.de, Internet: http://www.schweizerbart.de
Bernhard Harzer Verlag GmbH, Westmarkstraße 59/59a, 76227 Karlsruhe, Germany, Tel.: +49-721 944020, Fax: +49-721 9440230, e-mail: Info@harzer.de, Internet: www.harzer.de
Printed in Germany by Tutte Druckerei & Verlagsservice GmbH, 94121 Salzweg, Germany.

PFG – Jahrgang 2015, Heft 5
Inhaltsverzeichnis

Originalbeiträge

Beiträge aus Wissenschaft und Praxis

Mitteilungen

Zusammenfassungen der „Originalbeiträge“ und der „Beiträge aus Wissenschaft und Praxis“ (deutsch und englisch) sind auch verfügbar unter www.dgpf.de/neu/pfg/ausgaben.htm

PFG 2015 / 5, 0357–0372
Stuttgart, October 2015

Article

Accuracy of Laser Scanners for Measuring Surfaces made of Synthetic Materials

Grzegorz Lenda, Urszula Marmol & Grzegorz Mirek, Cracow, Poland

Keywords: terrestrial lidar, measurement error, material tests

Summary: Synthetics are a group of materials which, when observed using laser scanners, may cause additional measurement errors. These errors result from optical permeability, which may vary depending on the structure of the synthetic material. A laser beam which penetrates the material can be subject to numerous physical phenomena such as absorption, dispersion, full or partial reflection, refraction at the interface between two media, diffraction and interference that change the measured distance. As a result, additional measurement errors occur, independent of the known errors, when the beam is reflected from the outer surface of the material. Their occurrence is influenced by light transmission, density and internal structure of the synthetic material, its colour and thickness. The distance from the scanner, laser beam angle of incidence, temperature, scanner type (carrier wavelength), or even the distance between the synthetic material and its background are important as well. This study is devoted to examining these dependencies. Currently there are no studies distinguishing and examining synthetic materials as a separate group of materials that may interfere with distance measurements due to the phenomena that occur in their structure.

Zusammenfassung: *Genauigkeit von Laser-Scannern bei der Oberflächenmessung von synthetischen Materialien.* Synthetische Materialien können bei der Erfassung von Oberflächen mit Laserscannern zu zusätzlichen Messfehlern führen. Diese Fehler ergeben sich aus der optischen Durchlässigkeit, die in Abhängigkeit von der Struktur des synthetischen Materials variieren kann. Ein Laserstrahl, der in das Material eindringt, kann mehreren physikalischen Phänomenen, z. B. Absorption, Streuung, vollständige oder teilweise Reflexion, Refraktion an Grenzflächen zwischen zwei Medien, Beugung oder Überlagerung, unterworfen sein, welche die gemessene Distanz verändern. Als Ergebnis erhält man zusätzliche und von bisher bekannten Fehlerursachen unabhängige Messfehler, wenn der Strahl an einer aus synthetischem Material bestehenden Oberfläche reflektiert wird. Diese werden von der Lichtdurchlässigkeit, der Dichte und der inneren Struktur des synthetischen Materials beeinflusst. Die Distanz vom Scanner, der Auftreffwinkel des Laserstrahls, die Temperatur, der Scannertyp (Trägerfrequenz des Lasers) oder auch die Distanz der gescannten Oberfläche von Objekten, die sich aus Sicht des Sensors im Hintergrund befinden, sind ebenfalls von Bedeutung. Dieser Beitrag widmet sich der Untersuchung dieser Einflüsse. Bisher gibt es keine Studien, welche synthetische Materialen als eigene Gruppe von Materialen unterscheiden, welche in spezifischer Weise die Distanzmessung auf Grund ihrer inneren Struktur beeinflussen.

1 Introduction

Synthetic materials (materials consisting of synthetic polymers) are a group of materials which, when observed using laser scanners, may cause additional measurement errors. These errors result from the optical permeability, which may vary depending on the structure of the synthetic material. Existence of this phenomenon may be proved by the following experiment. One can measure a distance to a synthetic element, for example 2 mm – 3 mm thick, consisting of white

www.schweizerbart.de
DOI: 10.1127/pfg/2015/0273 1432-8364/15/0273 $ 4.00

Plexiglas or polystyrene, using any type of reflectorless range finder, then measure it again without changing the position of the element but with an identical element adhered to its back surface. The observed distance will be greater due to laser beam penetration through added layers of material. On the other hand, covering the front surface with a sheet of paper will prevent the laser beam from penetrating and result in a shorter measured distance. A laser beam penetrating the material may initiate a number of physical phenomena, changing the measured distance. As a result, additional measurement errors occur, independent of the already familiar errors that occur when the beam is reflected from the outer surface of the material. Even cursory tests of selected materials demonstrate that in some cases these errors can appear much bigger than the assumed accuracy of the scanner. Due to the growing use of synthetic elements in various branches of technology and construction, as well as the high prevalence of scanning techniques for the measurements of all types of structures (Berenyi et al. 2010, Hiremagalur et al. 2007, Holst et al. 2012, Johnson & Johnson 2012, Monserrat & Crosetto 2008, Salemi et al. 2008), a need arises to investigate the influence of these materials on errors of measured distances.

In the literature on examining the accuracy of laser scanners there have been no studies that address measurements to synthetic materials, although some of them indicate potential problems associated with measuring materials having a certain degree of transparency (Eren et al. 2009, Salemi et al. 2008, Voegtle et al. 2008). Generally, on the basis of several laser scanning studies (Abbas et al. 2013, Eren et al. 2009, Gottwald 2008, Kaasalainen et al. 2011, Kersten et al. 2009, Lee et al. 2010, Lichti & Jamtsho 2006, Polo et al. 2012, Soudarissanane et al. 2007) and those given below, it is known that the measurement accuracy is affected by several factors, including: the type of a scanner (pulse-based, phase-based), the precision of a scanning mechanism (laser footprint, accuracy and resolution of the horizontal and vertical angular encoders, the eccentricity of the scanning system), scanning geometry (beam angle of incidence, scanning distance), external conditions (lighting, humidity, temperature), and the properties of the scanned surface.

Considering the properties of the material, which this article focuses on, the research work carried out by Boehler et al. (2003) is worth mentioning. Their paper includes a series of tests for checking the quantitative and qualitative accuracy of points measured using nine laser scanners selected from different manufacturers. Among other things, the relation between surfaces of varying reflectivity and the accuracy of the acquired information was tested. The following samples made of various materials and in different colours were used: white paint (90 % and 80 % reflective), grey paint (40 % reflective), black paint (8 % reflective), metallic paint, various kinds of films. Measurements of different colour surfaces yielded good accuracy results. For the white surfaces, a deviation of zero was obtained. Also, the grey and black colours brought zero errors for most scanners. The situation was much worse in the case of different types of films, where errors from a few up to tens of millimetres occurred. Contradictory results were shown in Bucksch et al. (2007), where the bright surfaces gave much greater accuracy than the dark ones. The problem associated with material reflectance has been analysed in Clark & Robson (2004). The authors selected materials of standardized colours and textures, and scan them from various distances (4 m – 24 m) at the angles of 20°, 40° and 60°. The experimental results revealed systematic discrepancies in the recorded distances, depending on the type of the scanned surface. Colours which exhibit low reflectance, such as black or red, lead to longer distance measurements than the reference distance. The authors proposed a correction factor, reducing these systematic errors. A similar problem was presented in Pfeifer et al. (2008), where the authors focused on the signal energy returning to the receiver. It was hypothesized that this energy can be determined based on the observed range and intensity value. It was proven that it was possible to reproduce the reflectance of a given surface with the accuracy at the level of 6 %. Surface reflectance is also dealt with in Zámečníková et al. (2014b). The authors used the standard white colour (spectralon), which is the mate-

rial of almost perfect Lambertian reflectance, as well as cardboard boxes in varied colours. The materials were moved on a specially constructed trolley in the range of 1.1 m to 29.7 m at every 7.5 cm. The authors found that the obtained deviations depend not only on the range, but also on the signal strength.

Another study of the properties of the scanned objects was performed by Voegtle et al. (2008). This study used materials commonly applied on the façades of buildings, having different properties: colourful sheets and shades of gray, different kinds of wood, metal elements, plaster of various granularity, transparent films and materials with varying degrees of moisture. The authors' attention was drawn to the tests of partly transparent materials: errors ranged from 15 mm (for 35 % transparency) to 34 mm (for 5 % transparency).

It is not possible to analyse properties of the scanned material separately from the scanning geometry. Both the angle of the beam incidence and the distance have a significant effect on the resulting accuracy. In Soudarissanane et al. (2007) it was found that the measurement noise for a fibreboard and plywood painted white increases with increasing angles. The effect of the scanning angle on the resulting accuracy was also analysed in Soudarissanane et al. (2009) and Soudarissanane et al. (2011). An increase in the measurement noise with the increasing scanning angle was identified. The authors proposed a model which optimized the point position and corrected the influence of the angle. There was a significant improvement in the standard deviation, from the value of 3.25 mm to 2.55 mm. The influence of the scanning angle on the final accuracy was also presented in Zámečníková et al. (2014a). For the angles 100° – 65° and 50° – 45° the measured distances were longer than the reference distance, while in the range of 65° – 50° they were shorter. The authors did not explain the specific character of this phenomenon. Having eliminated the systematic factor, using a polynomial model, the values of standard deviations were significantly reduced.

From the point of view of the research results presented in our study, experiments with a metal plate were interesting. In Voegtle et al. (2008) the effect of the beam angle of incidence on the resulting accuracy was analyzed. Considering the values of the mean square errors, the following relation was noted: for the perpendicular direction of the beam incidence the errors are significantly larger than for smaller angles. A metal plate (aluminium, high reflectance) also appears in Zámečníková et al. (2014b). The authors noticed that small changes in the scanning angle (0.1°) result in 20 % changes in the signal strength, and thus to changes in the recorded deviations. The results presented in that paper confirmed that a higher reflectance results in larger errors for short distances, and for the distances exceeding 20 m their value decreases.

In conclusion, it can be said that the research hitherto conducted mainly analyzed the errors caused by the reflection of a laser beam from the outer surface of a material. Synthetic materials were neither tested nor distinguished as a separate group of materials which might distort the measurements of a distance due to their internal structure. Therefore, this work presents error analysis for distance measurements of the elements of this type.

The authors initially studied measurements to synthetic materials in Lenda & Marmol (2010) by testing the distance measurement deviations of reflectorless range finders for a few selected materials. It enabled the first conclusions on the factors influencing the distance measurement errors of synthetic materials, as well as to plan appropriate methodology for the implementation of research studies, taking into account a wider range of materials for laser scanners. The studies carried out in this paper present a wide range of issues. From the point of view of the users, this paper allows for a sufficient assessment of the impact of synthetic materials on the laser scanners' distance measurements.

2 Research Methodology

A laser beam in the structure of a synthetic material may be subject to a series of phenomena, such as absorption, dispersion, full or partial reflection, diffraction and interference, and refraction at the interface between two media (Feynman et al. 2001, Fowles 1989, Rees 1990, Trager 2007, Wandachowicz

2000). Depending on the type of the material, the influence of each of these properties varies with respect to the errors of the measured distance. On the basis of the tests carried out in Lenda & Marmol (2010), it was observed that the magnitude of these phenomena is affected mainly by factors such as the degree of light transmission, type of the synthetic material (chemical composition), density, thickness and the temperature of the material. The colour of the material is of some importance as well, which, however, was not included in the previously conducted research. According to these observations, a group of 16 materials was selected for testing. The analysis of 13 of these (Tab. 1), due to the similar properties of the materials and obtained results, turned out to be sufficient.

Plexiglas was the material with the biggest changes in measured distances during the range finder tests. Therefore, for this particular synthetic material, the most detailed tests were planned, taking into account its colour, thickness and light transmission. Other high density materials included: HIPS, Polystyrene and Polyolefin (rubber). Materials with low density were represented by foam synthetic materials: Styrofoam and Polyurethane foam. All tested materials, except for the coloured Plexiglas, were white or gray, which was favourable from the point of view of the range and accuracy of the reflectorless measurements. Plexiglas had a specified degree of light transmission. This parameter was unknown for the other materials. The tests associated with different thicknesses of the synthetic materials were performed for two materials: with high density, i.e. for Plexiglas, and with low density, i.e. for Styrofoam.

Temperature also influences the results of the reflectorless distance measurements. All materials were tested at two temperatures: at about 15 °C and at about 40 °C. The temperature of 15 °C (cold) was ambient temperature, and the temperature of 40 °C (warm) was reached by heating the materials with a portable heater. The temperature measurement was carried out using a Testo 830-T2 pyrometer.

The results of the reflectorless measurements are also affected by the incidence angle of the beam on the target. To assess the significance of this factor, basic tests were performed at the most favourable, normal incidence of the laser beam on the target (90°). For comparison, measurements were also carried out for the beam incidence at an angle of 45°. Materials with partial transparency placed at an angle increase the distance which the beam can travel within the structure of the material. Potentially, this could affect the increase in

Tab. 1: The materials tested.

No.	Material type	Colour	Thickness (mm)	Transparency (%)
1	Plexiglas (Polymethyl methacrylate)	red	5	30
2	Plexiglas	green	5	30
3	Plexiglas	blue	5	30
4	Plexiglas	white	5	30
5	Plexiglas	white	5	70
6	Plexiglas	black	5	30
7	Plexiglas	white	10	30
8	HIPS (High impact polystyrene)	white	5	-
9	Polystyrene	white	5	-
10	Styrofoam (Extruded polystyrene foam)	white	5	-
11	Styrofoam	white	10	-
12	Polyurethane foam	grey	10	-
13	Rubber (Polyolefin)	grey	5	-

the error values. On the other hand, due to the partial reflection of the beam from the surface of the material placed at an angle, the penetration of the interior of the material can be limited, which will reduce the value of the errors. For these reasons, it is difficult to find an analogy with other studies at varying angles of the beam incidence, contained in the existing literature.

Since our previous studies of reflectorless range finders presented the effect of a distance on the obtained errors associated with greater penetration of the material by the laser beam on shorter distances, tests of the scanners were carried out on the bases of three lengths: 5 m, 15 m and 50 m.

The procedure of determining the distance measurement deviations for each of the materials requires an explanation. We built a target of 20 cm × 30 cm for each material. Those targets were split into two halves of 20 cm × 15 cm each (Fig. 1). For the cardboard, which served as a reference, the distance deviation in relation to the original Leica reflective tape target had been predetermined – it equals 0.6 mm – taking into account the difference in thickness of the cardboard and tape target (Leica 2015). It was decided not to stick the tape target directly on the tested synthetic materials, due to a possibility of it being transmitted by the laser beam, which would enable the penetration into the structure of the synthetic material, distorting the results. The tested synthetic materials adhered directly to the opaque background. The planar target was scanned at a high resolution (2 mm density). Points near the boundaries of the two halves of the targets were removed from the cloud of points in order to obtain homogeneous sets of points. Based on the filtered data, a regression plane was determined for each of the fields,

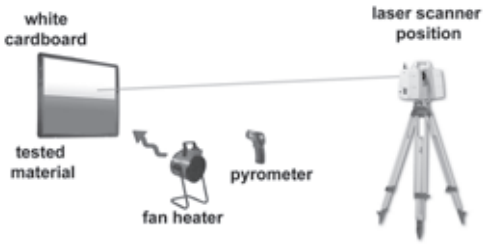

Fig. 1: Experimental setup.

and then the distance between them was compared, taking into account the thickness of the cardboard. The compared planes were created from two different point clouds, so they were not exactly parallel. The determination of the distance between them was carried out as follows: The regression planes have been fitted in the reference cloud and the test cloud. The dense point grid with a resolution of 1 point per 3 mm² has been interpolated on the test plane. Then the distances from all points of the sample of the reference plane have been determined, along the normal to that plane. Then the average distance has been calculated and taken as the distance between the planes. Such a method of determining the distance allowed eliminating inaccuracies associated with a slight rotation of both planes. The difference was the distance measurement deviation of the synthetic material with reference to the white cardboard, and, consequently, to the reflective tape. The deviation of the distance measurement of synthetic materials observed in this way (ΔD) is not an overall error of distance measurement. It is, however, an additional contribution, which should be added to the standard errors of a laser scanner, assuming reflection of a beam from the outer surface of the material. In addition, the precision (mp) of fitting the regression plane into a set of points representing the synthetic material, expressed by the RMS-error of the distances of the points from the regression plane was determined.

The tests were performed using two laser scanners with similar accuracy, but with a different carrier wavelength: Leica C10 and Riegl VZ-400. Basic data of these scanners with reference to the subject in question were presented in Tab. 2. The carrier wavelength is important especially when measuring targets of varying colours since spectral curves may differ even in the case of very similar materials (Toś 2014). The colour of the material may influence the absorption of beams with different wavelengths. It can also affect the measurement accuracy of synthetic materials in a varied manner, depending on the size of the inhomogeneity in their structure.

In the production process it is not always possible to obtain a uniform chemical composition and repetitive structure of synthetic ma-

Tab. 2: Selected parameters of the tested laser scanners.

	Leica C-10	Riegl VZ-400
Type	pulse-based	pulse-based
Accuracy of length measurement	4 mm (up to 50 m)	5 mm (up to 100 m)
Range	up to 350 m	up to 600 m
Carrier wavelength	532 nm	1550 nm
Beam divergence	0.24 mrad	0.35 mrad

terials. For this reason, comparative tests were performed for several materials (Plexiglas white, 5 mm thickness and 30 % transparency (hereinafter briefly stated with x mm/Y %), Polystyrene 5 mm, and Styrofoam 10 mm), taking into account the measurement of three samples of the same production lot, as well as the measurement to three samples of unknown origin. The tests were performed using the Leica C-10 scanner, at the baseline of 5 m, the distance between the laser scanner and the test material.

3 Results of Test Measurements

The results obtained from the conducted tests are shown in Tab. 3 (Leica C-10 scanner) and Tab. 4 (Riegl VZ-400 scanner). Due to highly ambiguous results (scattered data) of the measurements performed at the angle of 45° at the distances of 15 m and 50 m, they are not presented here. The diagrams presented in Figs. 2 and 3 were drawn based on these Tables. The measurement results of different samples of the same materials are included in

Tab. 3: Distance measurement deviations of the Leica C-10 scanner (ΔD = distance measurement deviations relative to the comparative model, mp = precision of fitting the regression plane for a synthetic material, tr. = transparency).

	Leica C-10	cold (mm)								warm (mm)						mean
		5m		5m / 45°		15m		50m		5m		15m		50m		ΔD
		ΔD	mp	ΔD	mp	ΔD	mp	ΔD	mp	ΔD	mp	ΔD	mp	ΔD	mp	(mm)
1	Plexiglas red, 5mm, 30% tr.	5.3	±3.9	-	-	4.4	±2.6	3.2	±3.8	3.4	±3.8	2.8	±2.4	2.9	±3.8	4
2	Plexiglas green, 5mm, 30% tr.	9.1	±1.4	6.3	±1.1	9.3	±1.4	6.9	±1.7	7.5	±1.4	8.1	±1.4	6.3	±1.7	8
3	Plexiglas blue, 5mm, 30% tr.	4.2	±2.8	4.0	±2.8	4.9	±2.3	3.7	±4.3	3.5	±2.8	3.3	±2.3	2.0	±4.4	4
4	Plexiglas white, 5mm, 30% tr.	8.5	±1.2	6.1	±0.7	8.1	±1.2	7.1	±1.3	7.4	±1.2	7.2	±1.6	6.9	±1.3	7
5	Plexiglas white, 5mm, 70%tr.	13.7	±1.3	10.4	±0.7	12.7	±1.4	10.1	±2.1	14.2	±1.3	12.3	±2.2	8.6	±2.1	12
6	Plexiglas black, 5mm, 30% tr.	4.4	±3	-	-	3.3	±2.9	2.0	±2.7	2.3	±3.1	2.1	±2.8	0.8	±2.7	2
7	Plexiglas white, 10mm, 30% tr.	11.6	±1.2	8.3	±0.7	10.2	±1.7	8.4	±1.3	9.1	±1.2	7.3	±1.4	6.8	±1.4	9
8	HIPS, 5 mm	4.2	±1.2	1.8	±0.7	3.4	±1.3	2.5	±1.2	3.4	±1.2	2.6	±1.3	2.1	±1.3	3
9	Polystyrene, 5mm	4.8	±1.2	3.4	±0.7	4.0	±1.3	2.1	±1.2	4.2	±1.2	3.4	±1.3	2.2	±1.2	3
10	Styrofoam, 5mm	2.1	±1.2	2.1	±0.8	2.1	±1.2	2.9	±1.2	2.3	±1.3	2.0	±1.3	3.1	±1.2	2
11	Styrofoam, 10mm	3.3	±1.3	2.5	±0.8	3.3	±1.2	3.1	±1.3	3.5	±1.3	3.0	±1.4	2.8	±1.4	3
12	Polyurethane foam, 10 mm	4.5	±1.2	3.7	±0.7	4.1	±1.3	3.5	±1.4	4.3	±1.2	4.5	±1.4	2.1	±1.6	4
13	Polyolefin (rubber), 5mm	0.9	±1.2	0.7	±0.8	0.7	±1.2	0.7	±1.3	0.3	±1.2	0.9	±1.5	0.3	±1.4	1

Tab. 4: Distance measurement deviations for the Riegl VZ-400 scanner.

	Riegl VZ-400	cold (mm)								warm (mm)						mean
		5m		5m / 45°		15m		50m		5m		15m		50m		ΔD
		ΔD	mp	ΔD	mp	ΔD	mp	ΔD	mp	ΔD	mp	ΔD	mp	ΔD	mp	(mm)
1	Plexiglas red, 5mm, 30% tr.	7.1	±1.6	4.3	±1.0	7.4	±2.6	6.6	±2.2	5.8	±1.4	6.4	±2.5	5.2	±2.4	6
2	Plexiglas green, 5mm, 30% tr.	7.5	±1.0	7.9	±0.8	6.8	±1.4	6.5	±1.7	6.4	±1.1	5.3	±1.4	5.4	±1.9	7
3	Plexiglas blue, 5mm, 30% tr.	10.2	±1.4	11.5	±1.2	9.9	±2.3	7.7	±4.3	7.5	±2.8	8.1	±2.7	6.4	±4.2	9
4	Plexiglas white, 5mm, 30% tr.	9.4	±1.1	7.6	±0.7	8.5	±1.2	6.9	±1.3	8.0	±1.2	7.8	±1.4	6.9	±1.4	8
5	Plexiglas white, 5mm, 70%tr.	15.2	±1.7	11.4	±1.5	13.7	±3.0	12.3	±2.5	12.0	±1.3	10.1	±3.3	10.5	±2.6	12
6	Plexiglas black, 5mm, 30% tr.	10.5	±1.1	5.9	±0.7	-	-	-	-	8.8	±1.6	-	-	-	-	8
7	Plexiglas white, 10mm, 30% tr.	13.3	±0.9	9.8	±0.9	12.2	±1.4	10.5	±1.5	10.3	±1.2	10.5	±1.8	8.3	±1.6	11
8	HIPS, 5 mm	7.3	±1.1	3.5	±0.8	7.0	±1.1	5.2	±1.3	5.4	±1.7	4.9	±1.2	4.1	±1.4	5
9	Polystyrene, 5mm	6.3	±1.2	4.5	±1.0	6.2	±1.3	5.1	±1.3	4.5	±1.3	4.2	±1.3	4.0	±1.3	5
10	Styrofoam, 5mm	2.9	±1.1	2.7	±0.8	3.8	±1.2	3.2	±1.2	3.0	±1.4	4.2	±1.3	2.9	±1.3	3
11	Styrofoam, 10mm	5.2	±1.6	6.3	±1.0	5.3	±1.7	7.2	±1.3	4.9	±1.5	5.8	±1.5	6.4	±1.3	6
12	Polyurethane foam, 10 mm	11.1	±1.1	7.8	±0.9	11.7	±1.3	13.8	±1.4	10.6	±1.2	12.1	±1.4	13.2	±1.7	11
13	Polyolefin (rubber), 5mm	1.4	±1.1	1.2	±0.9	1.0	±1.4	0.8	±1.3	0.9	±1.3	0.4	±1.8	0.2	±1.5	1

Tab. 5. During the tests with the VZ-400 scanner, it was noticed that synthetic materials were not directly adhering to the background, but they stood out approximately 2 cm – 3 cm behind it. This resulted in a significant deterioration in the distance measurement deviation for some materials. The measurements were repeated and, for comparison, Tab. 6 shows the results for the background adhering and not adhering to the synthetic material.

The precision of fitting the regression plane for the reference cardboard was similar for both scanners and it was ±1.2 mm for 90° beam incidence angles, and ±0.8 mm for the 45° incidence angles, with the scatter for these values reaching a maximum of ±0.2 mm.

Tab. 5: Distance measurement deviations of the samples for selected materials: A1–A3 – sample material from the same production lot, B1–B3 – sample material from unknown production lots, Leica C-10 scanner, distance 5 m.

	Plexiglas white, 5 mm, 30% transparency (mm)	Polystyrene, 5 mm (mm)	Styrofoam 10 mm (mm)
A 1	8.5	4.8	3.3
A 2	8.1	4.6	3.9
A 3	8.8	5.1	4.2
B 1	8.5	4.8	3.3
B 2	6.9	4.7	5.2
B 3	11.8	6.4	2.8

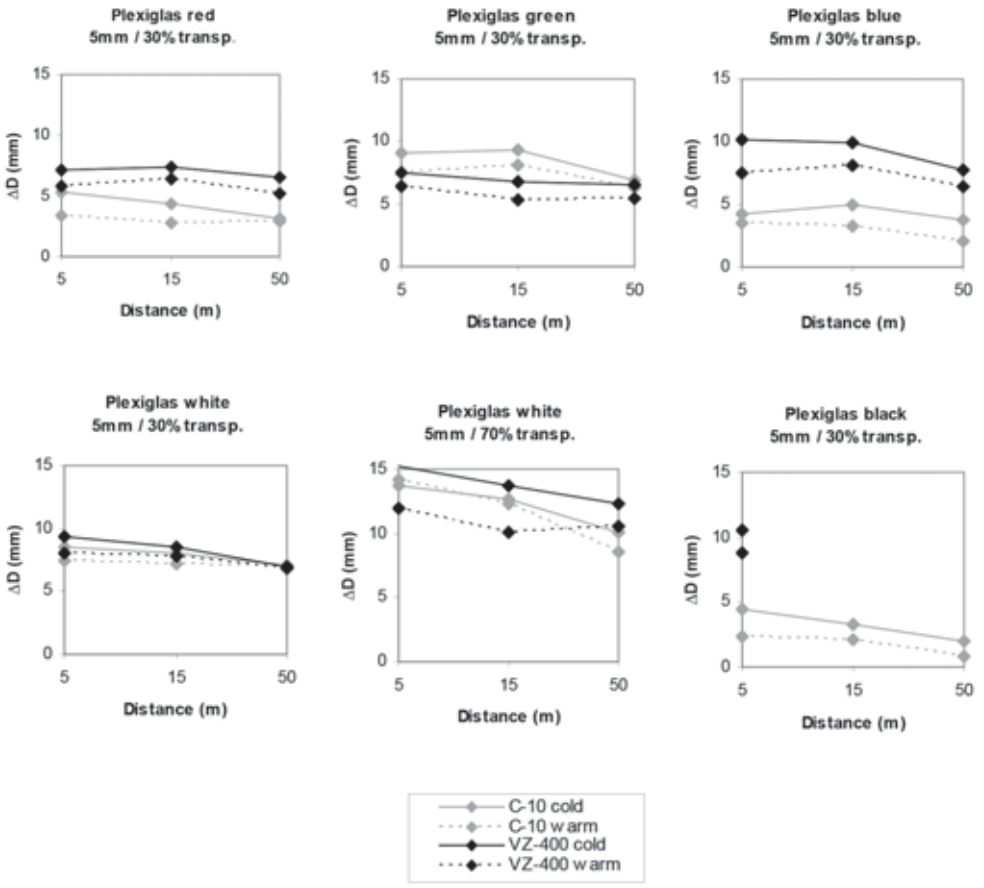

Fig. 2: Distance measurement deviations for the materials 1–6, ΔD – distance measurement deviations relative to the comparative model.

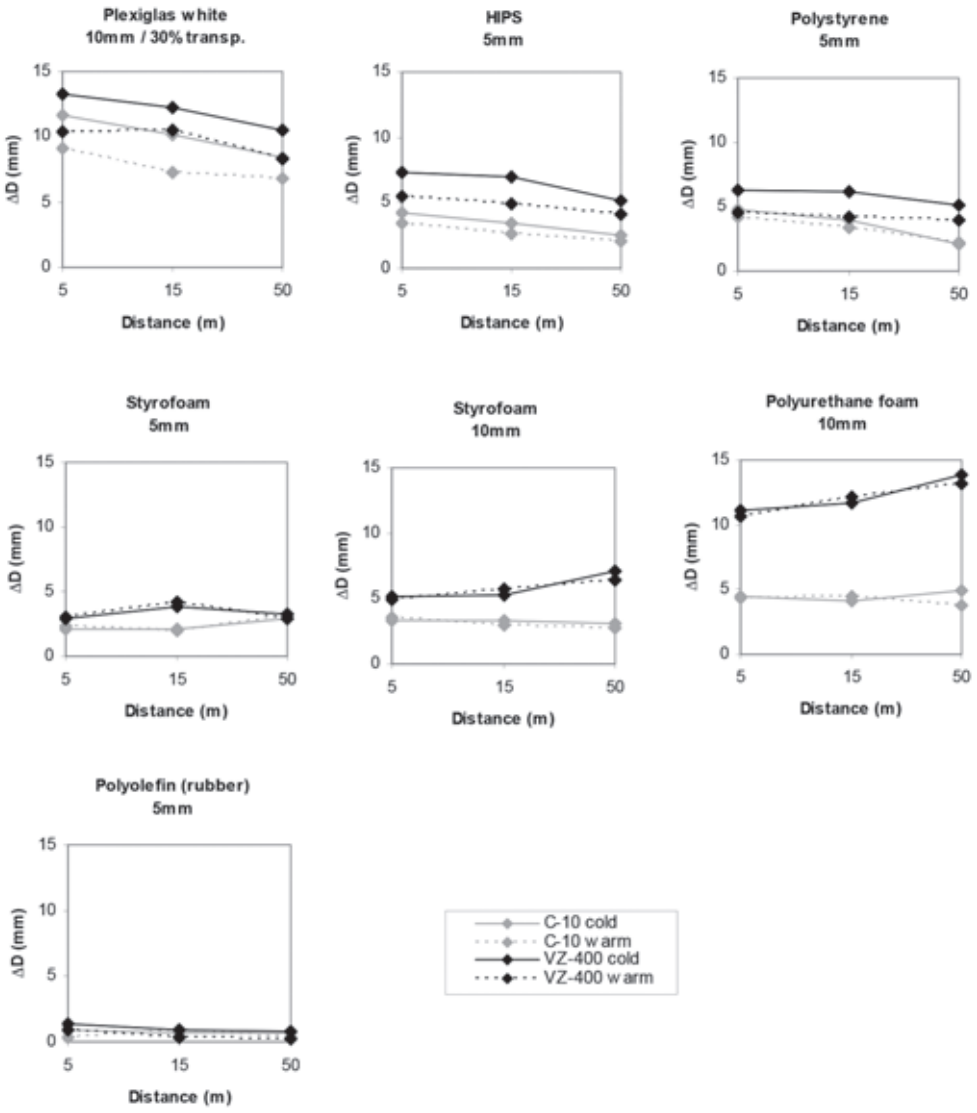

Fig. 3: Distance measurement deviations for the materials 7–13, ΔD – distance measurement deviations relative to the comparative model.

Tab. 6: Comparison of the distance measurement deviations of the VZ-400 scanner for various locations of the synthetic material background. Test 1: The background adhering to the rear surface of the synthetic material. Test 2: The background placed approximately 2 cm – 3 cm behind the synthetic material. Comparison for the 5 m distance (tr. – transparency).

	Riegl VZ-400	5m			
		Test 1 (mm)		Test 2 (mm)	
		ΔD	mp	ΔD	mp
1	Plexiglas red, 5mm, 30% tr.	7.1	±1.6	31.6	±2.3
2	Plexiglas green, 5mm, 30% tr.	7.5	±1.0	24.7	±1.6
3	Plexiglas blue, 5mm, 30% tr.	10.2	±1.4	19.3	±1.5
4	Plexiglas white, 5mm, 30% tr.	9.4	±1.1	16.1	±1.0
5	Plexiglas white, 5mm, 70%tr.	7.4	±1.7	27.8	±2.5
6	Plexiglas black, 5mm, 30% tr.	10.5	±1.1	-	-
7	Plexiglas white, 10mm, 30% tr.	13.3	±0.9	17.3	±1.1
8	HIPS, 5 mm	7.3	±1.1	7.0	±1.1
9	Polystyrene, 5mm	6.3	±1.2	6.1	±1.4
10	Styrofoam, 5mm	2.9	±1.1	3.3	±0.9
11	Styrofoam, 10mm	5.2	±1.6	5.6	±1.4
12	Polyurethane foam, 10 mm	11.1	±1.1	13.8	±1.7
13	Polyolefin (rubber), 5mm	1.4	±1.1	1.9	±1.0

4 Analysis of the Results

The assessment of the results was divided into several categories, resulting from the properties of the material itself, the conditions in which it was found, and the tested instrument. The analyses included the following categories: type of material (light transmission, density and internal structure, colour, thickness), distance, angle of incidence, temperature, type of scanner (carrier wavelength), and distance of the synthetic material from the background. Some phenomena were especially noticeable for the shortest measurement distance (5 m), at low temperature of the material (15 °C), which is explained later in the text. Therefore, during the comparisons, we will frequently refer to the results obtained under such conditions as the "basic" conditions.

4.1 *Light Transmission*

This is the primary factor affecting the distance measurement of synthetic materials. If the laser beam is not able to penetrate into the structure of the synthetic material, there are no changes in the measured distance in comparison with the reference cardboard. Such a situation can be observed only for one of the tested materials, i.e. opaque rubber (Polyolefin). Regardless of the conditions, the distance measurement error for this material did not exceed the value of 2 mm, usually remaining at the level of about 1 mm, unlike other materials, where a certain degree of transparency allowed for the occurrence of additional phenomena affecting the distance measurement. The changes in the distance observed for them ranged from about 2 mm to 15 mm. The influence of transmission was clearly visible when comparing the two samples of Plexiglas white, with a transmission of 30 % and 70 %. Mean deviations for the material with lower transmission were approximately 7 mm (C10) and 8 mm (VZ400), and 12 mm for larger transmission (C10 and VZ400). For both scanners, taking into account comparable materials (5 mm thickness, white colour), the largest deviations occurred for Plexiglas, which had a significant light transmission. Other materials were measured with mean deviations within

the range of 1 mm – 3 mm (C10) and 1 mm – 5 mm (VZ400). For the C10 scanner, Plexiglas with 70 % transmission caused a slight deterioration in the precision of fitting the regression plane relative to other materials (up to ca. ±2 mm). For the VZ400 scanner, the fitting precision for this material decreased in some cases to ca. ±3 mm.

4.2 *Density and Internal Structure*

The studies covered two groups of materials with large differences in density and internal structure. The first one included materials with a continuous structure (Plexiglas, HIPS, Polystyrene, Polyolefin), and the second one included foamed materials (Styrofoam, Polyurethane Foam). In the foamed materials the beam was subject to changes, alternately in fragments of the material and in air chambers. Foamed materials were measured with smaller deviations in relation to the thickness of the material than their continuous counterparts. This could be assessed by comparing the measurement deviations of Polystyrene and Polystyrene Foam (Styrofoam) (5 mm) in basic conditions: Polystyrene: 4.8 mm (C10), 6.3 mm (VZ400) and Styrofoam: 2.1 mm (C10), 2.9 mm (VZ400). The foamed material achieved deviations of approximately half that size. It is interesting that for some materials, especially for Plexiglas, the measurement deviations were larger than the thickness of the material itself. Examples under basic conditions were Plexiglas white 5 mm / 30 % – 8.5 mm (C10), 9.4 mm (VZ400), Plexiglas white 5 mm / 70 % – 13.7 mm (C10), 15.2 mm (VZ400). During the tests, the materials adhered directly to the opaque background, so that the beam, having passed through the material, did not have a possibility of incidence on other targets. The values of the deviations, therefore, must have resulted from additional phenomena associated with the beam propagation in the structure of the material. They might be related, among others, to the repeated refraction or the reflection of a beam. In addition, the refractive index depends on the internal structure of materials. If it is not homogeneous, and the inhomogeneity has dimensions greater than the wavelength, the refractive index will be subject to changes. Comparing the measurements results performed with the C10 scanner to various samples of materials from the same production lot (Tab. 5), a stable level of deviations for Plexiglas white 5 mm / 30 % – (8.1 mm – 8.8 mm) and Polystyrene 5 mm / 30 % – (4.6 mm – 5.1 mm) is noticeable. For the foamed material, 10 mm Styrofoam, the relative differences are larger – (3.3 mm – 4.2 mm). When comparing samples of these materials originating from different production lots, possibly from different manufacturers, the results look somewhat different. Differences for 5 mm Polystyrene increased to 4.7 mm – 6.4 mm. For other materials, the relative differences were nearly doubled: 10 mm Styrofoam: 2.8 mm – 5.2 mm, Plexiglas white 5 mm/30 %: 6.9 mm – 11.8 mm. Therefore, the type of a material and its internal structure have a significant impact on the level of the measurement deviations. At the same time, this influence is difficult to determine accurately due to variations in the production.

4.3 *Colour*

The colour of the synthetic material significantly influences the measurement deviations. A sample Plexiglas was tested under basic conditions using the same parameters regarding thickness and permeability. Then, the deviations resulting from the changing colour of the material were within 4.2 mm – 9.1 mm (C10) and 7.1 mm – 10.5 mm (VZ400). For both scanners, the differences between the extreme values of the deviations had a factor of 1.5 to 2. As only a few selected colours were tested, a discrepancy may be even larger under real conditions. The colour of the material strongly influenced the absorption of beams with different wavelengths. Due to the fact that two scanners emitting laser radiation of different carrier wavelengths, 532 nm (C 10) and 1550 nm (VZ400), were selected for this experiment, the differences in the values of the deviations for the same colours were clearly noticeable. Under basic conditions, for the C10 scanner, the smallest deviations were observed for the following colours: blue: 4.2 mm, black: 4.4 mm, and red: 5.3 mm. It is interesting that, at the same time, for those colours

the lowest precision of fitting a regression plane were obtained: blue: ±2.8 mm, black: ±3.0 mm, red: ±3.9 mm. Larger deviations were observed for white (8.5 mm) and green (9.1 mm), with better precision of fitting the plane: white ±1.2 mm, green ±1.4 mm. The VZ400 scanner demonstrated the smallest deviations for red (7.1 mm) and green (7.5 mm), and the largest for the blue (10.2 mm) and black (10.5 mm) colours. Therefore, for green, blue and black, the dependencies observed for the C10 scanner were inverted. In basic conditions, the precision of fitting the regression plane were at a low level for all colours (±1.0 mm – ±1.6 mm). For the test configurations other than the basic ones, the deviations for red and blue increased. The colour of the synthetic material in combination with its light transmittance is therefore a very important factor determining the value of the distance measurement deviations.

4.4 *Thickness*

The effect of the thickness of the synthetic material was assessed based on two samples of materials (Plexiglas 30 %, 5 mm and 10 mm, and Styrofoam, 5 mm and 10 mm). Under basic conditions, the measurement deviations using the C10 scanner for Plexiglas ranged from 8.5 mm to 11.6 mm, and for the VZ400 scanner from 9.4 mm to 13.3 mm. For Styrofoam, the deviations for the C10 scanner ranged from 2.1 mm to 3.3 mm, and for the VZ400 scanner from 2.9 to 5.2 mm. The deviations were different for each sample and scanner, and were within the limits of 36 % – 79 %, at 100 % change in thickness of the material. Greater differences were observed for the foamed material of low density, i.e. for Styrofoam 57 % – 79 %, while for Plexiglas they amounted to 36 % – 41 %. As Styrofoam in practice had a thickness greater than 5 mm or 10 mm, this could translate into relatively large measurement deviations. In view of the fact that colour has also a strong influence on the deviations of the measurements on Plexiglas the deviations could reach values higher than the thickness of the material itself. This happened in more than half of the cases for the C10 scanner and all of the cases for the VZ400. This could also be recognized with other synthetic materials measured with the VZ400 scanner, e.g. HIPS and Polystyrene. The dependencies related to the thickness of the synthetic material are therefore significant, nonlinear, and for better assessment it would be advisable to carry out more extensive tests.

4.5 *Distance*

Dependencies resulting from the variable distance of the target are easiest to evaluate from the diagrams in Figs. 2 and 3. For most materials, the deviations are reduced with increasing distance. The differences between the results for the distances of 5 m and 15 m do not exhibit this phenomenon clearly, i.e. sometimes the deviations even increase. However, the differences between the results at the distances of 5 m and 50 m exhibit a certain tendency and reach the values of up to 3.5 mm. The increasing tendency of the deviations was observed for two foamed materials: Styrofoam (10 mm) and Polyurethane Foam for the VZ400 scanner. Deviations decreasing with distance are contrary to current experiments for reflectorless instruments. Moreover, the equipment manufacturers themselves inform about increasing deviations with increasing distance. However, this phenomenon can be explained by a reduced ability of radiation to penetrate the material which, at the larger distance, has a lower energy density at the surface of the synthetic material. In this way, the scale of the phenomena described above is limited. Due to the fact that the largest deviations were observed at short distances, the 5-meter baseline was set as the “basic” condition. With the increasing distance there was no significant increase in the precision of fitting the regression plane.

4.6 *Incidence Angle*

Studies related to the varying incidence angles of the beam yielded inconclusive results. The tests were carried out at the angle of 45° without the materials being heated. The results for the distances of 15 m and 50 m did not demonstrate any systematic order, the measurement

deviations just increased or decreased in a random manner. This was associated with significant decrease of precision of fitting the regression planes with up to several millimetres.

The ambiguous test results at greater distances could have resulted from the variable reaction of fragments of the materials to the illumination at an angle. At a greater distance where the density of the radiation energy at the sample surface is smaller, the non-homogeneity of the material could have determined the phenomenon of partial reflection from the surface of the inclined sample, changing the degree of the material penetration by the beam. This is particularly visible for the blue Plexiglas measured with the C10 scanner at a distance of 15 m (Fig. 4). The left figure presents a sample scanned at the angle of 90°, and the right one at the angle of 45°. Significant losses in the point cloud (front view, right side) together with highly scattered individual points (top view, right side) are visible in the latter case.

For this reason, only the results for the distance of 5 m are presented, because they seemed not to be subject to blunders. With the decreasing angle of the beam incidence (from the standard 90° to 45°), for the C10 scanner, a decreasing measurement deviation of up to about 3 mm in almost all the cases was observed. This was related to the decrease in the deviations of fitting the regression plane from about ±1.2 mm to ±0.7 mm on an average. Similar observations were made in Voegtle et al. (2008), where it was also found that with a decreasing incidence angle, the deviation decreased. However, in Soudarissanane et al. (2007), for some materials an opposite tendency was observed. It was also confirmed by the previous research of the authors associated with the tests of reflectorless range finders (Lenda & Marmol 2010). Similar relations were observed for the instrument VZ400, where the deviations decreased by more than 4 mm. However, for some materials (Plexiglas green and blue, 10 mm Styrofoam), a slight, about 1 mm increase in the deviations occurred. The precision of fitting the regression plane were also subject to a decrease an average of about ±1.2 mm to ±1.0 mm. In our experiments, at the angle of incidence of 45°, the materials Plexiglas red and black were immeasurable for the Leica scanner. Based on the obtained results and the results of other researchers, it was apparent that the angles of incidence affect the measured distance. The tests exhibited a decrease in the deviations at more acute angles of the beam incidence – which may be the result of reduced penetration by laser beam due to partial reflection from the surface of the sample at incidence angle of 45°.

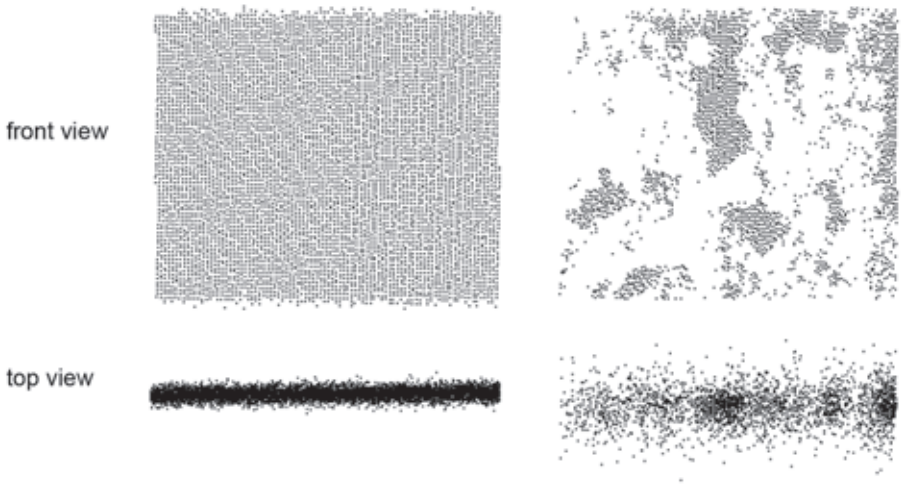

Fig. 4: Point clouds obtained from blue Plexiglas with the C10 laser scanner at 15 m distance. Sample scanned at 90° incidence angle on the left and 45° incidence angle on the right; above: front views of the materials, below: top views of the materials.

4.7 *Temperature of the Material*

The influence of the temperature is easiest to assess from the diagrams contained in Figs. 2 and 3. A decrease in the deviations for the non-foamed materials (except rubber) related to the temperature growth is quite clear, as well as its lack for the foamed materials. Non-foamed synthetic materials, when heated, generate deviations that are smaller by about 1 mm – 3 mm (C10) and by about 1 mm – 4 mm (VZ400) than cold ones. Continuous materials, having no air bubbles in their structures, exhibited susceptibility to heat. This phenomenon could be explained by the thermal expansion of materials and the related lower density of synthetic materials, reducing the refractive index value. However, since the change in the volume of the synthetic materials when heated was negligible, other factors related to temperature, unnoticed by the authors, must have affected the reduction of the measurement deviations. Due to the fact that larger deviations were observed for cold targets, low temperature was adopted as another "basic" conditions.

4.8 *Scanner Type*

In this category, the carrier wavelength of the laser, different for the two scanners (532 nm (C10) and 1550 nm (VZ400)) should be distinguished. The light of various wavelengths is absorbed in a different manner by the colours and materials of a different size and ordering of the molecules. Taking into account all 13 tested materials, almost all of the tests demonstrated slightly higher deviation values for the VZ400 scanner. This dependency could have been expected when comparing the precision parameters of both instruments.

4.9 *Distance between Synthetic Material and the Background*

The location of the background of the tested material is of great importance to the measured distance of some synthetic materials. If it is close, just a few centimetres from the synthetic material, a laser beam, after being transmitted through the material, can be reflected by the background, causing significant changes to the obtained results, of up to several centimetres. For some synthetic materials it does not really matter (HIPS, Polystyrene, Styrofoam, Polyolefin), for others these changes may be small (Polyurethane foam). For some of the materials (Plexiglas, especially with small thickness) it may, however, result in very significant discrepancies. The observed increase in the deviations for different colours of 5 mm Plexiglas, under basic conditions, ranged from 71 % (white) to as much as 345 % (red), reaching the values of up to 32 mm. It was combined with a slight increase in the plane fitting precision. The dependencies associated with the colours were quite different from the ones observed for the background adhering to the synthetic material. The loss of accuracy related to a complete passage of light through the synthetic material may thus result in obtaining significant, unpredictable values. Further studies, taking into account various distances between the synthetic material and the background, may foster interesting results.

5 Summary

The paper analyses a number of factors affecting the distance measurement of synthetic materials. The most important of these is optical permeability, which induces other phenomena occurring within the material structure. Some of them may have a significant impact on the obtained results, e.g. degree of permeability, type of material, colour in combination with a carrier wavelength of the laser radiation, and thickness. The effects of other factors seem to be less significant, but noticeable and systematic such as distance and temperature of the material. The angle of the beam incidence is also relevant. Synthetic elements may therefore exhibit shifts of several, sometimes over a dozen millimetres in the point cloud relative to other objects. Especially when they not adhere to the other materials, shifts in some cases (Plexiglas) may increase to several centimetres. In some cases, measurement deviation of the synthetic material can affect the accuracy of the entire scanned structure. This may happen

when spatial markers in the form of Styrofoam balls are used to connect neighbouring scans. As it was demonstrated by our experiments, the error for Styrofoam increases significantly with its thickness, and therefore covering such balls with opaque lacquer should be considered. Some of the tests yielded inconclusive or questionable results (incidence angle), which may have resulted from the methodology, dependent upon the occurrence of additional phenomena, which the authors had not anticipated. The factors that interfere with the results of the research studies may include for example: additional lighting, reflections of the beam from the surrounding elements, type of the synthetic material background and the manner of its adherence to the sample. The deviations resulting from a complete passage of light through the synthetic material and the reflection of a beam from the background located at a certain distance from the material may reach significant values. In general, due to a large number of factors affecting the distance measurements and their mutual configurations, it is difficult to tabulate distance measurement deviations for specific synthetic materials. The situation is made worse by an average repeatability of their production. This study draws attention to the problem, allowing estimating the scale of the existing dependencies.

Acknowledgements

This work has been made within scientific research program no. 11.11.150.005, 11.11.150.949.

References

Abbas, M.A., Setan, H., Majid, Z., Chong, A.K., Idris, K.M. & Aspuri, A., 2013: Calibration and Accuracy Assessment of Leica ScanStation C10 Terrestrial Laser Scanner. Developments in Multidimensional Spatial Data Models. – Lecture Notes in Geoinformation and Cartography **10:** 33–47.

Berenyi, A., Lovas, T. & Barsi, A., 2010: Terrestrial laser scanning – civil engineering applications. – International Archives of the Photogrammetry, Remote Sensing and Spatial Information Sciences, Commission V Symposium **38** (5): 80–85, Newcastle, United Kingdom.

Boehler, W., Bordas, V.M. & Marbs, A., 2003: Investigating laser scanner accuracy. – 19th CIPA International Symposium, Antalya, Turkey.

Bucksch, A., Lindenbergh, R. & van Ree, J., 2007: Error budget of terrestrial laserscanning: Influence of the intensity remission of the scan quality. – III International Scientific Congress GeoSiberia, Novosibirsk, Russia.

Clark, J. & Robson, S., 2004: Accuracy of measurements made with a CYRAX 2500 laser scanner against surfaces of known color. – Survey Review **37** (294): 626–638.

Eren, G., Aubreton, O., Meriaudeau, F., Secades, S., Fofi, D., Naskali, A.T., Truchetet, F. & Ercil, A., 2009: A 3D Scanner for Transparent Glass. Image Analysis and Processing. – International Conference on Image Analysis and Processing (ICIAP) 2009, Lecture Notes in Computer Science (LNCS) **5716:** 519–527.

Feynman, R.P., Leighton, R.B. & Sands, M., 2001: The Feynman Lectures on Physics. – PWN, Warszawa, Poland.

Fowles, G.R., 1989: Introduction to Modern Optics. – Dover Publications, Mineola, NY, USA.

Gottwald, R., 2008: Field Procedures for Testing Terrestrial Laser Scanners (TLS) – A Contribution to a Future ISO Standard. – Integrating Generations, FIG Working Week **2008:** 1–14, Stockholm, Sweden.

Hiremagalur, J., Yen, K., Akin, K., Bui, T., Lasky, T. & Ravani, B., 2007: Creating standards and specifications for the use of laser scanning in caltrans projects. – AHMCT (Advanced Highway Maintenance & Construction Technology Research Center) Research Report, University of California at Davis, California Department of Transportation, Davis, CA, USA.

Holst, C., Zeimetz, P., Nothnagel, A., Schauerte, W. & Kuhlmann, H., 2012: Estimation of Focal Length Variations of a 100-m Radio Telescope's Main Reflector by Laser Scanner Measurements. – Journal of Surveying Engineering **138** (3): 126–135.

Johnson, W. & Johnson, A., 2012: Operational Considerations for Terrestrial Laser Scanner Use in Highway Construction Applications. – Journal of Surveying Engineering **138** (4): 214–222.

Kaasalainen, S., Jaakkola, A., Kaasalainen, M., Krooks, A. & Kukko, A., 2011: Analysis of Incidence Angle and Distance Effects on Terrestrial Laser Scanner Intensity: Search for Correction Methods. – Remote Sensing **3** (10): 2207–2221.

Kersten, T.P., Mechelke, K., Lindstaedt, M. & Sternberg, H., 2009: Methods for Geometric Accuracy Investigations of Terrestrial Laser

Scanning Systems. – PFG – Photogrammetrie, Fernerkundung, Geoinformation **2009** (4): 301–315.

Lee, I.S., Lee, J.O., Park, H.J. & Bae, K.H., 2010: Investigations into the influence of object characteristics on the quality of terrestrial laser scanner data. – KSCE Journal of Civil Engineering **14** (6): 905–913.

Leica, 2015: http://www.allenprecision.com/survey/robotic-total-stations/accessories/prisms/60x60mm-reflective-tape-20-pack/ (19.7.2015).

Lenda, G. & Marmol, U., 2010: Accuracy of reflectorless range finders for the measurements of objects made form synthetic materials (polish). – Pomiary Automatyka Kontrola **11:** 1280–1286.

Lichti, D.D. & Jamtsho, S., 2006: Angular resolution of terrestrial laser scanners. – The Photogrammetric Record **21** (114): 141–160.

Monserrat, O. & Crosetto, M., 2008: Deformation measurement using terrestrial laser scanning data and least squares 3D surface matching. – ISPRS Journal of Phtotogrammetry & Remote Sensing **63:** 142–154.

Pfeifer, N., Höfle, B., Briese, C., Rutzinger, M. & Haring, A. 2008: Analysis of the backscattered energy in terrestrial laser scanning data. – International Archives of the Photogrammetry and Remote Sensing and Spatial Information Science (IAPRS) **37** (B5): 1045–1051.

Polo, M.E., Felicísimo, A.M., Villanueva, A.G. & Martínez-del-Pozo, J.A., 2012: Estimating the Uncertainty of Terrestrial Laser Scanner Measurements. – IEEE Transactions on Geoscience and Remote Sensing **50** (11): 4804–4808.

Rees, W., 1990: Physical principles of remote sensing. – Cambridge University Press, UK.

Salemi, G., Achilli, V. & Boatt, G., 2008: 3D virtual modelling of a gothic stained-glass panel. – The International Archives of the Photogrammetry, Remote Sensing and Spatial Information Sciences **37** (B5): 297–302.

Soudarissanane, S., van Ree, J., Bucksch, A. & Lindenbergh, R., 2007: Error budget of terrestrial laser scanning: influence of the incidence angle on the scan quality. – 3D-NordOst, Berlin.

Soudarissanane, S., Lindenbergh, R., Menenti, M. & Teunissen, P.J.G., 2009: Incidence angle influence on the quality of terrestrial laser scanning points. – ISPRS International Archives of the Photogrammetry, Remote Sensing and Spatial Information Sciences **38-3/W8:** 183–188.

Soudarissanane, S., Lindenbergh, R., Menenti, M., Teunissen, P.J.G., 2011: Scanning geometry: Influencing factor on the quality of terrestrial laser scanning points. – ISPRS Journal of Photogrammetry and Remote Sensing **66** (4): 389–399.

Toś, C., 2014: The possibilities of using the terrestial scanning data for classification of rocks in limestone mine 'Czatkowice'. – Reports on Geodesy and Geoinformatics **97:** 80–90.

Trager, F., 2007: Springer Handbook of Lasers and Optics. – Springer.

Voegtle, T., Schwab, I. & Landes, T., 2008: Influence of different materials on the measurements of terrestrial laser scanner. – The International Archives of the Photogrammetry, Remote Sensing and Spatial Information Sciences **37** (B5): 1061–1066.

Wandachowicz, K., 2000: Wyznaczanie rozkładu luminancji we wnętrzach z uwzględnieniem kierunkowo-rozproszonych charakterystyk odbiciowych materiałów (Determination of the luminance distribution in the interiors taking into account the characteristics of the directional-diffuse reflectance materials). – doctoral dissertation, Poznań, Poland.

Zámečníková, M., Neuner, H. & Pegritz, S., 2014a: Influence of the Incidence Angle on the Reflectorless Distance Measurement in Close Range. – INGEO 2014 – 6th International Conference on Engineering Surveying: 257–262, Prague, Czech Republic.

Zámečníková, M., Wieser, A., Woschitz, H. & Ressl, C., 2014b: Influence of surface reflectivity on reflectorless electronic distance measurement and terrestrial laser scanning. – Journal of Applied Geodesy **8** (4): 311–325.

Addresses of the Authors

Grzegorz Lenda, Ph.D. & Urszula Marmol, Ph.D., AGH University of Science and Technology, Faculty of Mining Surveying and Environmental Engineering, Cracow, Mickiewicza 30, Poland, Tel.: +48-12-617-23-14, -26, Fax: +48-12-617-50-76, e-mail: {grzenda}{entice}@agh.edu.pl

Grzegorz Mirek, Ph.D., Cracow University of Technology, Faculty of Environmental Engineering, Cracow, Warszawska 24, Poland, Tel.: +48-12-628-21-87, e-mail: gmirek@pk.edu.pl

Manuskript eingereicht: Februar 2015
Angenommen: Juli 2015

PFG 2015 / 5, 0373–0380
Stuttgart, October 2015

Article

Local Prototype Space-based Band Selection for Hyperspectral Subpixel Analysis

Hamed Gholizadeh, Bloomington, IN, USA, Barat Mojaradi & Mohammad Javad Valadan Zoej, Tehran, Iran

Keywords: Dimension reduction, prototype space, subpixel analysis, hyperspectral data

Summary: In this paper, two unsupervised local band selection (BS) methods in the prototype space (PS) for improving subpixel analysis performance are proposed. Here, the PS is a two dimensional space which is constituted of the target spectrum and that of the local background. The proposed methods benefit from local background characterization through image clustering. These BS methods select the discriminative bands in two ways: 1) selecting the bands which form a convex hull in the PS, and 2) using a cluster-based approach in the PS to select bands. An experiment applied to real-world hyperspectral data showed that the proposed BS methods improve the performance of constrained energy minimization (CEM) and adaptive matched filter (AMF) subpixel detection methods in terms of the number of false alarms.

Zusammenfassung: *Verbesserung der Subpixelanalyse von Hyperspektraldaten durch Verwendung des so genannten „Prototyp-Raumes“.* Mit dem Ziel einer verbesserten Subpixel-Analyse werden in diesem Artikel zwei unüberwachte Methoden zur Auswahl spektraler Bänder im so genannten „Prototype-Raum“ (PS) untersucht. In dieser Studie ist der PS ein zweidimensionaler Raum, der aus den Signalen des Targets sowie des lokalen Hintergrunds aufgebaut ist. Dabei erweist sich die Ableitung des lokalen Hintergrunds mittels Clusteranalyse als geeignet. Zwei Methoden werden vorgeschlagen, die geeigneten Bänder abzuleiten: 1) Auswahl der Bänder, die im PS das Gerüst der konvexen Hülle bilden, und 2) Auswahl der Bänder aus den Ergebnissen einer Clusteranalyse im PS. Die Anwendung anhand eines Hyperspektraldatensatzes zeigt, dass die beiden vorgeschlagenen Methoden zur Auswahl spektraler Bänder die Ergebnisse der Constrained Energy Minimization (CEM) und des Adaptive Matched Filter (AMF), zweier Detektionsmethoden von Targets auf Subpixelebene, hinsichtlich ihrer Falsch-Positiv-Rate verbessern.

1 Introduction

Algorithms used in hyperspectral applications can be divided into four categories (Manolakis et al. 2001): target/anomaly detection, change detection, classification, and spectral unmixing. Very high spectral resolution of hyperspectral data increases discrimination between materials with similar spectral responses (Melgani & Bruzzone 2004). There are, however, several challenges in hyperspectral data analysis including the curse of dimensionality. Therefore, automatic analysis of hyperspectral data is not a trivial task (Melgani & Bruzzone 2004). One possible way to mitigate these problems is dimension reduction of the hyperspectral data. Dimension reduction methods can be grouped into two main categories: 1) feature selection, i.e. band selection, and 2) feature extraction. The former identifies a subset of the original bands without affecting their physical meanings, whereas in the latter case each feature is a combination of the original data (Kaewpijit et al. 2003). In target detection applications maintaining the physical meaning of the bands is mandatory.

www.schweizerbart.de
DOI: 10.1127/pfg/2015/0275
1432-8364/15/0275 $ 2.00

Therefore, in this paper, we focus on band selection (BS) methods. Because spectral signatures of targets are affected by the materials in their neighbourhood rather than by the globally extracted endmembers (Matteoli et al. 2009), the proposed methods aim at applying BS in a local background. We refer the interested reader to Jain & Zongker (1997), Bruzzone & Serpico (2000), Mitra et al. (2002), and Chang & Wang (2006) for more details on BS methods.

In this paper, we present two unsupervised local BS methods to improve target detection performance. To this end, we first project the data into the prototype space (PS) (Mojaradi et al. 2009). To select informative bands in the PS, two solutions are proposed: 1) choosing the bands which form a convex hull, and 2) choosing the bands by band clustering in the PS. After dimension reduction, the constrained energy minimization (CEM) (Harsanyi 1993), adaptive cosine/coherent estimate (ACE) (Kraut et al. 2005) and adaptive matched filter (AMF) (Robey et al. 1992) target detectors are used. The ultimate goal of the proposed BS methods is improving target/background discrimination via minimizing the redundancy in the hyperspectral image (HSI) data. Experiments were conducted on a hyperspectral image acquired by the HyMap sensor and the results confirmed the validity of the proposed methods. This paper is outlined as follows. The proposed methods are described in section 2. Dataset description and final results are discussed in section 3. In section 4, we present the conclusions and final remarks.

2 PS-based Band Selection

Conventional target detectors, e.g. CEM, ACE, and AMF, characterize the background globally in full dimension, i.e. using all bands. However, by using the proposed BS algorithms, target detection methods can be applied locally to data with reduced dimension. In fact, the idea behind these algorithms is that for a given target and a local background, a set of bands can be selected. The main processing steps of the proposed methods are shown in Fig. 1 and described in the following subsections.

2.1 *Pre-Processing*

1) *Image partitioning*: The image is partitioned into eight equal sub-images (Fig. 1a). The justification for partitioning the image is due to two operational considerations: (1) to avoid memory shortage in the processing systems, and (2) to make the implementation of the proposed methods in parallel processing systems feasible.
2) *Data clustering in each partition*: The proposed methods are applied locally. Each image partition is made up of several endmembers. So, each partition is clustered using the fuzzy c-means (FCM) method (Bezdek et al. 1984) (Fig. 1b). The number of clusters in each partition is determined by the signal subspace dimension using the HySime method (Bioucas-Dias & Nascimento 2008).
3) *PS formation*: In this paper, we propose the use of the PS for band representation. Each point in the PS corresponds to one band in the spectral space. Moreover, target detection is a binary hypothesis testing problem in which we choose between two possible cases: (1) target is present, or (2) target is absent, i.e. the pixel under test is considered as background. Therefore, the dimension of the PS can be set to two. Target spectrum forms the first dimension of the PS. To represent the second dimension of the PS, i.e. background, the mean spectrum of each cluster in a given image partition is used (Fig. 1c). In sum, the PS can be formed using the spectra of target and background (Fig. 1d).

To illustrate the idea behind PS, assume that the spectral signatures of target and background are shown as column vectors t and m, respectively. To form the PS, we use the concatenation of t and m which is expressed as E.

$$E = \left[\boldsymbol{t}\ \boldsymbol{m}\right]^{\mathrm{T}} = \begin{bmatrix} t_1 & \dots & t_l \\ m_1 & \dots & m_l \end{bmatrix}, \tag{1}$$

where l is the number of bands. Each column of E corresponds to one point in the PS.

Since we follow a partition-based approach for BS, the PS is formed for each cluster in a given partition. For instance, if a partition is made up of five clusters, then five separate PSs for each target will be formed.

2.2 *Band Selection*

Two BS methods in the PS are proposed: 1) convex-based method, and 2) cluster-based method (Fig. 1e).

1) Convex-based BS: "A set S is convex if for every pair of points $p, q \in S$, the line segment pq is contained in S" (Latecki et al. 1995), and the smallest convex set containing S is called a convex hull. Inspired by this definition, we select discriminative bands in the PS, which are the points forming the convex hull. In the convex-based BS, non-boundary points of the convex region in the PS, i.e. bands inside the convex hull, can be considered as combinations of the points which form the convex hull. We refer the interested reader to Andrew (1979) for a more detailed introduction to convex hulls in two dimensions.

2) Cluster-based BS: In this method, the bands in the PS are clustered by the FCM method. Having clustered the bands, the band with the shortest Euclidean distance to the cluster centroid is chosen as the representative of that band cluster. The issue that needs to be addressed is the number of band clusters. To estimate the number of band clusters, a cluster validity index (CVI) is used. CVIs estimate the number of clusters by comparing the clustering performance for different number of clusters. To estimate the number of band clusters in the PS, the Calinski-Harabasz (CH) index (Caliński & Harabasz 1974) is employed. The CH index can be written as

$$CH = \frac{B}{W}\frac{(n-k)}{(k-1)}, \tag{2}$$

where B and W are the between-cluster and within-cluster sum of squares, respectively, n is the number of points, and k is the number of clusters (Caliński & Harabasz 1974). Maximum value of the CH index determines the optimal number of clusters. In other words, one possible approach

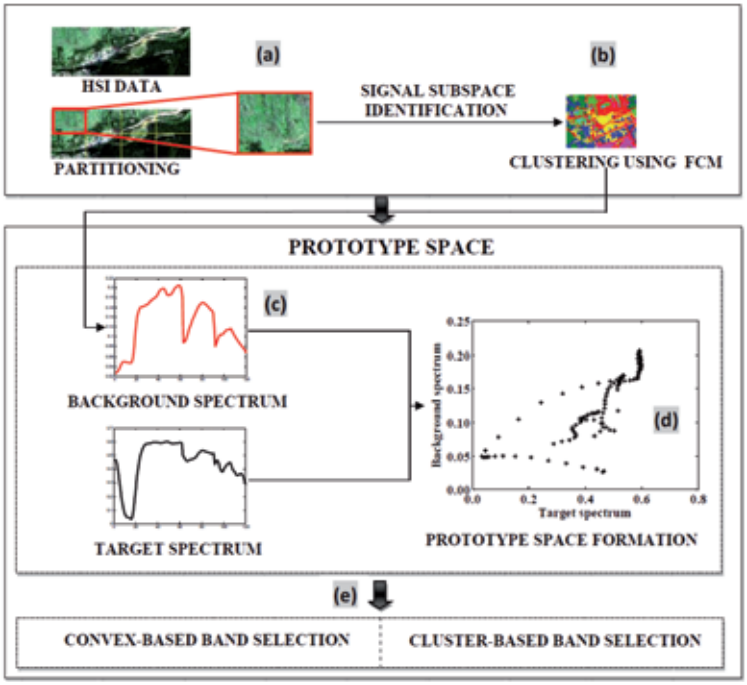

Fig. 1: Block diagram of the proposed local band selection approaches in the PS: (a) image partitioning, (b) data clustering, (c) determining the background spectra, (d) prototype space formation, and (e) band selection.
Note: only one instance of the background spectra, target spectra, and PS are shown here.

to determine the number of band clusters (k) is to find a k, $1 > k \leq M$, with the largest CH value. For our experiment, the upper bound (M) was set equal to the estimated signal subspace dimension in each image partition. It is also noteworthy that the CH index is used when the number of bands is not pre-determined. The cluster-based BS method can also be straightforwardly used for application with pre-determined number of bands by simply skipping the application of the CH index.

The ultimate goal of the proposed BS methods is to characterize a local background which guarantees discrimination of all targets from their surroundings. So, the union of the selected bands for all targets in each cluster is taken as the final set of bands for that cluster. The merit of the proposed BS methods is their unsupervised nature, i.e. they do not need any prior knowledge except the target spectrum.

3 Experimental Results

3.1 *Dataset Description*

To test the proposed BS methods, a HyMap reflectance data of Cooke City, MT, USA acquired in 2006 with the spatial resolution of 3 metres is used (Snyder et al. 2008). The image size is 280 pixels × 800 pixels and the number of bands in the original dataset is 126 (before pre-processing) covering the 0.45 µm – 2.5 µm region with 15 nm – 20 nm-wide bands. It should be noted that in this study noisy bands were removed from the original data. Several fabric panels, i.e. targets, were placed in the study area during data acquisition (see Fig. 2). Target characteristics are reported in Tab. 1. As can be seen, the size of some of these fabric panels is less than the spatial resolution of the data. The dataset also includes the spectral library of the target panels in the study area.

3.2 *Band Selection*

As an illustration of BS in the PS, selected bands for target F3 (1 m × 1 m) are shown in Fig. 3 (these bands correspond to one of the image clusters). The spectrum of the pixel containing target F3 (1 m × 1 m) as well as the mean spectrum of its eight neighbouring pixels are shown in Fig. 4. As can be seen, the high degree of similarity between the spectrum of the pixel containing target F3 and that of the neighbouring pixels can hamper robust detection, so selecting optimal bands is of vital importance.

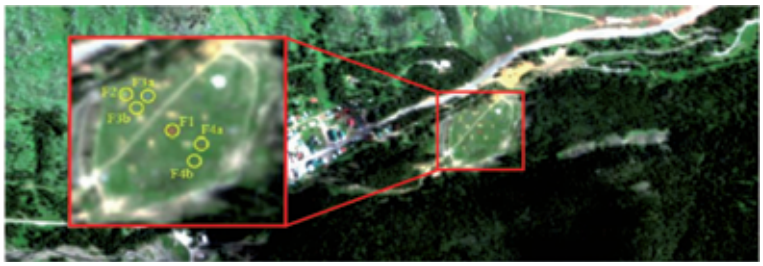

Fig. 2: True colour representation of the HyMap dataset. The red box represents the target area.

Tab. 1: Target characteristics in the HyMap image.

Target name	Fabric	Number of fabric panels	Size
F1	Red cotton	1	3 m × 3 m
F2	Yellow nylon	1	3 m × 3 m
F3	Blue cotton	2	2 m × 2 m, 1 m × 1 m
F4	Red nylon	2	2 m × 2 m, 1 m × 1 m

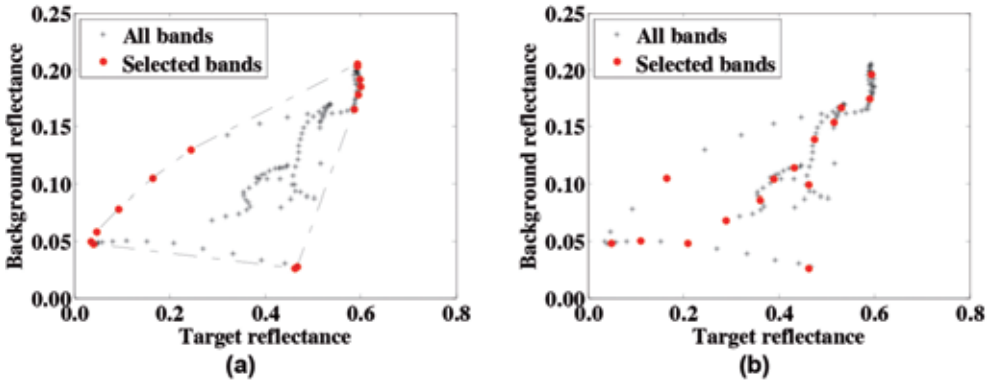

Fig. 3: An illustration of the selected bands in the PS: (a) convex-based band selection, and (b) cluster-based band selection. Red dots show the selected bands.

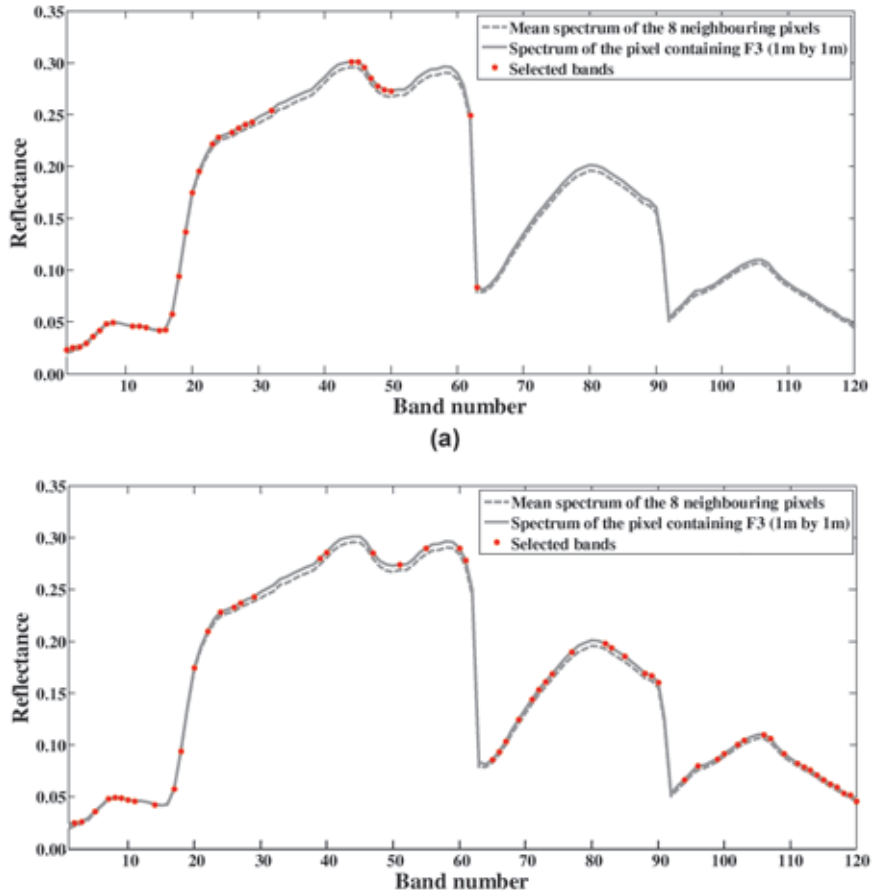

Fig. 4: Representing selected bands in the spectral space: (a) convex-based band selection, and (b) cluster-based band selection. Red dots show the selected bands.

The results from the convex-based method (Fig. 4a) show that all 34 selected bands fall within the bands 1 to 63 even though there are bands in other regions of the spectrum which may support more target/background separation. To alleviate this problem, a cluster analysis of the bands in the PS is applied and correlated bands are represented by clusters in the PS. Having clustered the bands by FCM, a band with minimum Euclidean distance to each cluster centre is selected. In FCM, the number of iterations and the weighting exponent are set to 100 and 2, respectively. In total, 58 bands are selected (see Fig. 4b). Distribution of the selected bands in the spectral space indicates that unlike the convex-based method, the cluster-based method finds a set of bands which maximize the overall discrimination between the target and background in all regions of the spectrum and thus the physical structure of the spectrum is preserved. The run time of the convex-based method and the cluster-based method on an Intel Core2 Duo 2.53 GHz processor with 4 GB of RAM is 9 and 172 seconds, respectively. This indicates high computational cost of the cluter-based method.

3.3 *Detection Evaluation*

To investigate the impact of the proposed BS methods on target detection performance, the CEM, ACE, and AMF algorithms are employed. These algorithms are developed for the case that the only available knowledge is the signature of the targets.

The performance of target detectors can be evaluated using the receiver operating characteristic (ROC) curve. The number of target pixels in the dataset used in this study is limited; therefore, results obtained from the ROC curve are not reliable. Consequently, to evaluate the detection performance, we use the approach proposed by Matteoli et al. (2011), which counts the number of false alarms (#FAs) for each target. Target detection results obtained from the CEM, ACE, and AMF detectors using the proposed BS methods and without BS, i.e. full dimension, are reported in Tab. 2. In this table, the #FAs for three scenarios are given: 1) no dimension reduction, i.e. using all bands, 2) using the convex-based method, and 3) using the cluster-based method. Due to random behaviour of the FCM algorithm at its first iteration, it may behave differently from run to run. Consequently, the median of 30 runs of the cluster-based method is presented here.

As is evident from Tab. 2, dimension reduction improves the detection performance of CEM and AMF detectors. In all experiments, the cluster-based method achieves lower or the same #FAs compared to the convex-based BS. This may be due to the fact that the cluster-based BS selects the discriminative bands in

Tab. 2: Detection results in terms of #FAs for CEM, ACE, and AMF methods (#FA = number of false alarms, CEM = constrained energy minimization, ACE = adaptive cosine / coherent estimate, AMF = adaptive matched filter).

Target	BS method	#FAs of each detection method		
		CEM	ACE	AMF
F1	Full dimension	14	0	13
	Convex-based	0	0	13
	Cluster-based	0	0	3
F2	Full dimension	0	0	0
	Convex-based	0	1	0
	Cluster-based	0	0	0
F3	Full dimension	29	0	100
	Convex-based	3	0	13
	Cluster-based	0	0	2
F4	Full dimension	20	0	20
	Convex-based	8	1	12
	Cluster-based	0	0	1

all regions of the spectrum. The cluster-based method shows the best performance by reducing the total #FAs from 63 to 0 for CEM, and 133 to 6 for AMF. It should be noted that the #FAs of the ACE detector is 0 without dimension reduction. Regarding the size of the targets, they can be divided into two groups: 1) easy targets, i.e. targets F1 and F2, and 2) difficult targets, i.e. targets F3 and F4. In case of easy targets, two BS methods yield perfect detection results with low #FAs. For difficult targets, higher #FAs is obtained, especially after applying the convex-based BS. In sum, by examining the obtained results we can conclude that: 1) the cluster-based method is more robust than the convex-based method and results in lower #FAs; however, its computational cost is higher, and 2) compared to the convex-based method, the cluster-based method identifies more discriminative bands.

4 Conclusion

In this paper, two local BS methods for improving detection performance were proposed. Conventional target detection algorithms have two main shortcomings: 1) they characterize the background globally, and 2) they use all bands of the HSI data. To resolve the first issue, the image was partitioned, and then each partition was clustered using FCM. These image clusters were used to characterize the background locally. To overcome the second shortcoming, two new BS methods in the PS were proposed. The first BS method forms a convex hull in the PS to select discriminative bands, whereas the second method clusters the bands in the PS to reduce the dimensionality of the data. Detection results revealed that both methods were able to select discriminative bands to improve the performance of CEM and AMF detection methods. In particular, the cluster-based method yielded the best detection results in terms of the number of false alarms.

Acknowledgement

The authors express their deepest gratitude to Dr. John Kerekes (Rochester Institute of Technology) for providing the HyMap dataset.

References

Andrew, A.M., 1979: Another efficient algorithm for convex hulls in two dimensions. – Information Processing Letters **9** (5): 216–219.

Bezdek, J.C., Ehrlich, R. & Full, W., 1984: FCM: The fuzzy c-means clustering algorithm. – Computers & Geosciences **10** (2): 191–203.

Bioucas-Dias, J. & Nascimento, J., 2008: Hyperspectral Subspace Identification. – IEEE Transactions on Geoscience and Remote Sensing **46** (8): 2435–2445.

Bruzzone, L. & Serpico, S.B., 2000: A technique for feature selection in multiclass problems. – International Journal of Remote Sensing **21** (3): 549–563.

Caliński, T. & Harabasz, J., 1974: A dendrite method for cluster analysis. – Communications in Statistics-theory and Methods **3** (1): 1–27.

Chang, C.I. & Wang, S., 2006: Constrained band selection for hyperspectral imagery. – IEEE Transactions on Geoscience and Remote Sensing **44** (6): 1575–1585.

Harsanyi, J.C., 1993: Detection and classification of subpixel spectral signatures in hyperspectral image sequences. – Ph.D. dissertation, Department of Electrical Engineering, University of Maryland, Baltimore County, USA.

Jain, A. & Zongker, D., 1997: Feature selection: Evaluation, application, and small sample performance. – IEEE Transactions on Pattern Analysis and Machine Intelligence **19** (2): 153–158.

Kaewpijit, S., Moigne, J.L. & El-Ghazawi, T., 2003: Automatic reduction of hyperspectral imagery using wavelet spectral analysis – IEEE Transactions on Geoscience and Remote Sensing **41** (1): 863–871.

Kraut, S., Scharf, L.L. & Butler, R.W., 2005: The adaptive coherence estimator: A uniformly most-powerful-invariant adaptive detection statistic. – IEEE Transactions on Geosciences on Remote Sensing **53** (2): 427–438.

Latecki, L., Rosenfeld, A. & Silverman, R., 1995: Generalized convexity: CP_3 and boundaries of convex sets. – Pattern Recognition **28** (8): 1191–1199.

Manolakis, D., Siracusa, C. & Shaw, G., 2001: Hyperspectral subpixel target detection using the linear mixing model. – IEEE Transactions on Geoscience and Remote Sensing **39** (7): 1392–1409.

Matteoli, S., Acito, N., Diani, M. & Corsini, G., 2009: Local approach to orthogonal subspace-based target detection in hyperspectral images. – First Workshop on Hyperspectral Image and Signal Processing: Evolution in Remote Sensing (WHISPERS): 1–4.

Matteoli, S., Ientilucci, E.J. & Kerekes, J.P., 2011: Operational and performance considerations of radiative-transfer modeling in hyperspectral target detection. – IEEE Transactions on Geosciences and Remote Sensing **49** (4): 1343–1355.

Melgani, F. & Bruzzone, L., 2004: Classification of hyperspectral remote sensing images with support vector machines. – IEEE Transactions on Geoscience and Remote Sensing **42** (8): 1778–1790.

Mitra, P., Murthy, C.A. & Pal, S.K., 2002: Unsupervised feature selection using feature similarity. – IEEE Transactions on Pattern Analysis and Machine Intelligence **24** (3): 301–312.

Mojaradi, B., Abrishami-Moghaddam, H., Zoej, M.J.V. & Duin, R.P., 2009: Dimensionality reduction of hyperspectral data via spectral feature extraction. – IEEE Transactions on Geoscience and Remote Sensing **47** (7): 2091–2105.

Robey, F.C., Fuhrmann, D.R., Kelly, E.J. & Nitzberg, R., 1992: A Cfar adaptive matched filter detector. – IEEE Transactions on Aerospace and Electronic Systems **28** (1): 208–216.

Snyder, D., Kerekes, J., Fairweather, I., Crabtree, R., Shive, J. & Hager, S., 2008: Development of a web-based application to evaluate target finding algorithms. – IEEE International Geoscience and Remote Sensing Symposium (IGARSS), Vol. **2:** II-915–II-918.

Addresses of the Authors:

Hamed Gholizadeh, Department of Geography, Indiana University, 701 E. Kirkwood Ave., Bloomington, IN 47405, USA, Phone: 812-855-6303, Fax: 812-855-1661, e-mail: hgholiza@indiana.edu

Barat Mojaradi, School of Civil Engineering, Iran University of Science and Technology, Tehran, Iran, P.O. Box: 16765-163, Phone: +98-21-77240399, Fax: +98-21-77240398, e-mail: mojaradi@iust.ac.ir

Mohammad Javad Valadan Zoej, Faculty of Geodesy and Geomatics Engineering, K.N. Toosi University of Technology, Tehran, Iran, P.O. Box: 15875-4416, Phone: +98-21-88786212, Fax: +98-21-88786213, e-mail: valadanzouj@kntu.ac.ir

Manuskript eingereicht: March 2015
Angenommen: Juli 2015

PFG 2015 / 5, 0381 – 0393
Stuttgart, October 2015

Report

Generation of TIR-attributed 3D Point Clouds from UAV-based Thermal Imagery

PATRICK WESTFELD, DAVID MADER & HANS-GERD MAAS, Dresden

Keywords: Unmanned aerial vehicle, thermal infrared imaging, calibration, structure from motion, 3D point cloud

Summary: This contribution investigates the possibility to efficientl reconstruct 3D scene geometry purely from thermal image data by using structure from motion techniques. The images are acquired by a low-cost, lightweight thermal camera mounted on an octocopter platform. The result is a 3D point cloud containing geometric information plus thermal attributes. Such a dataset may be valuable for building energy evaluation, where existing geospatial data may thus be enriched with thermal information.
The paper gives an overview of the automatic data processing chain and also considers aspects of geometric thermal camera calibration. For an extensive practical test, a raster pattern was fl wn, capturing 15,000 thermal images of the façades of a large building complex. To validate the geometric quality of the results, the point cloud was aligned to a terrestrial laser scanning 3D model of the scene. With a precision in the order of 25 mm, related to an object dimension of 50 m × 50 m × 20 m, the analysis of the model differences substantiated the geometric potential of thermal cameras in SfM tools.

Zusammenfassung: *Generierung von thermalen 3D-Punktwolken aus UAV-gestützten Wärmebildkameradaten*. Diese Arbeit untersucht das Potential von einzig auf Wärmebilddaten basierenden Structure-from-Motion Ansätzen zur effiziente 3D-Objektrekonstruktion. Getragen von einer Oktokopter-Flugroboterplattform wurden die Bilddaten mit einem preiswerten, kompakten thermischen Sensor aufgenommen. Zusätzlich zur Raumkoordinate enthält die resultierende 3D-Punktwolke eine thermische Information für jeden Objektpunkt. Vor allem im Bereich der energetischen Bewertung von Gebäuden kann diese Kombination von Geometrie und Thermografi von Interesse sein. Im Beitrag behandelt werden neben der Prozesskette zur automatischen Datenverarbeitung auch Aspekte der geometrischen Kalibrierung einer Wärmebildkamera. Im Rahmen eines umfangreichen praktischen Experiments wurden die Fassaden eines weitläufige Gebäudekomplexes rasterförmig abgefloge und ca. 15.000 Wärmbilder aufgenommen. Die Registrierung der erzeugten 3D-Punktwolke zu einem terrestrischen Laserscannermodell ermöglichte die Validierung der geometrischen Qualität der Ergebnisse. Mit 3D-Objektkoordinatenabweichungen in der Größenordnung von 25 mm, bezogen auf eine Objektgröße von 50 m × 50 m × 20 m, konnte das geometrische Potential in der Auswertung von Wärmebildkameradaten mit SfM-Werkzeugen belegt werden.

1 Introduction

Efficien energy handling is playing an increasingly important role in economy. Energy efficien y is clean, particularly favourable and immediately available. Taking diminishing resources and increasing prices for raw materials into consideration, energy efficien y forms one pillar of the energy revolution (KOHLER et al. 2013). European legislation requires an energy efficien y increase of 20 % by 2020 (2012/27/EU). In order to realize the directive, the German federal government offers incentives for individual energetic redevelopment of residential property, such as building envelope insulation or window replacements.

www.schweizerbart.de
DOI: 10.1127/1432-8364/2015/0274
1432-8364/15 /0274 $ 3.50

Heat loss from buildings can easily be visualized by thermograms. The common way in practice is that energy consultants acquire thermal infrared (TIR) images from individual buildings using hand-held thermal cameras. The TIR data are interpreted visually during on-site inspections, leading to recommendations for restructuring measures. This procedure is rather time-consuming and cost-intensive. Furthermore, a sharing and pooling of knowledge and data is impeded. However, it would be desirable – especially for the survey and assessment of larger areas like streets of houses, districts or even complete cities – to enrich spatial information stored in a geographic information system (GIS) with thermal attributes.

Several studies deal with the combination of thermal measurements and geometric data. The contribution of HOEGNER et al. (2007) focuses on the extraction and integration of façade textures from low resolution infrared image sequences. LAGÜELA et al. (2011b) and GONZÁLEZ-AGUILERA et al. (2012) describe approaches to multi-sensor registration of TIR images and terrestrial laser scanner (TLS) data. In these approaches, common features are extracted in both datasets to combine thermographic and geometric data in a joint thermographic 3D model. In BANNEHR et al. (2013), data from an airborne laser scanner, a hyperspectral and a thermal camera were fused in order to extract urban parameters like roof materials or geometric information. HOEGNER et al. (2013) present a method for the co-registration of time-of-fligh (TOF) camera generated 3D point clouds and TIR images. In HOEGNER & STILLA (2015), the relative orientation of terrestrial TIR image sequences from different views is estimated and in the fina analysis used to detect 3D building façade objects. In RUDOL & DOHERTY (2008), a technique is introduced which allows the detection and geolocalization of human bodies in thermal and colour imagery, acquired during several flight with an unmanned aerial vehicle (UAV). In PECH et al. (2013), urban heat islands are detected, monitored and analyzed. PECH et al. (2013) use RGB and thermal images, simultaneously captured by two cameras mounted on an UAV, to generate multi-temporal thermal orthophotos. IWASZCZUK et al. (2012) use aerial TIR image sequences for the detection of weak spots in building insulation by findin the best fi between a given 3D building model and the acquired TIR images. MAURIELLO & FROEHLICH (2014) give initial thoughts on how to automate the 3D reconstruction process of building façades from UAV-based collected thermal images.

The data for this study was captured by a thermal imaging camera onboard a UAV. This platform is part of a flee of unmanned aerial vehicles which are equipped with different sensors like laser scanner, RGB camera, near infrared camera and thermal camera. The fly ing robots have been designed and built in the course of the project ADFEX (Adaptive Federative 3D Exploration of Multi Robot Systems). Information on the entire project can be found on http://www.adfex.eu/.

The paper investigates the possibility to efficientl reconstruct 3D scene geometry purely from thermal image data by using structure from motion techniques. The paper gives an overview of the automatic data processing chain and also considers aspects of geometric thermal camera calibration. The results of the work presented here are TIR-attributed dense 3D point clouds of building façades. The paper is also focusing on the accuracy potential of thermal cameras in 3D point cloud generation through SfM.

The UAV sensor system is presented in section 6.2. The thermal sensor has to be calibrated firstl for accurate temperature measurements and secondly to correct for geometric errors affecting the optical imaging process (section 3). The data acquisition process to capture the façades of the courtyard of a building complex is described in section 4. Similar to the work of MAURIELLO & FROEHLICH (2014), this publication investigates the possibility to efficientl reconstruct camera poses and 3D scene geometry purely from overlapping thermal image sequences by using structure from motion (SfM) techniques. The necessary processing steps are treated in section 5. A critical analysis of the accuracies in 3D point cloud and single 3D points is given in 6. Finally, section 7 summarizes the work.

Fig. 1: (a) CAD model of an octocopter UAV sensor platform equipped with a thermal imaging camera FLIR A65. (b) Colour-coded thermal image of 640 pixel 512 pixel.

2 Sensor Systems

Any object surface having a temperature above absolute zero emits, reflect or transmits thermal radiation. The energy emitted is a measure for surface temperature and may be detected by suitable sensors such as cooled photon detectors and uncooled thermal detectors, DERENIAK & BOREMAN (1996).

In this study, we used a low-cost thermal imaging camera FLIR A65 which is based on an uncooled microbolometer array. The thermal sensor is sensitive in the infrared range between 7.5 µm and 13 µm. It produces thermal images of 640 pixel × 512 pixel with 17 µm pixel size (Fig. 1b) at 30 fps with a thermal sensitivity of less than 50 mK in a range of −40 °C to +160 °C. A fi ed 13 mm wide-angle lens (45° × 37°) provides a suitable fiel of view for the application at hand. The compact and lightweight camera body (106 mm×40 mm×43 mm; 200 g) enables an integration on a payload-restricted UAV.

The FLIR A65 is mounted on a multi-rotor flyin platform Cadmic Goliath Coax 8 (Fig. 1a). This 4-arm copter with eight rotors is part of an UAV fleet designed and used for 3D exploration tasks in urban environments. More detailed specification on the UAV platform are given in KLIX et al. (2014).

3 Thermal Camera Calibration

In order to achieve accurate and reliable measurements, a radiometric and geometric calibration of the thermal imaging sensor is necessary. Therefore, the model parameters for the temperature calculation as well as the imaging process have to be determined.

3.1 *Radiometric Calibration*

The formula to convert a 14 bit object signal S, acquired during frame grabbing, to a temperature value T (in K) is (FLIR 2012):

$$T = \frac{B}{\log(R \cdot (S - O)^{-1} + F)} \qquad (1)$$

The conversion parameters R, B, F and O are determined by pointing the camera at objects with known temperature. The black body infrared calibration source PYROTHERM CS 110 is used as a reference. During calibration, thermal image data are acquired in a range of −10 °C to +50 °C in steps of 10 K, and the four unknown radiometric calibration parameters are estimated by regression analysis. The a-posteriori standard deviation for measuring the absolute temperature of a black body within the specifie range of temperature can be stated with 70 mK (FLIR 2012). However, this level of accuracy can usually not be achieved in fiel applications due to differing emissivities and reflections

3.2 *Geometric Calibration*

The geometric camera model used here is slightly different from the one commonly used in photogrammetry (LUHMANN et al. 2006). It refers to a concept taken from computer vision (HARTLEY & ZISSERMAN 2004), to which the SfM tools used in section 5 are related.

Deviations between the ideal geometric projection model and the actual camera geometry have to be modeled to exhaust the accuracy potential of the image data. The imaging geometry of a thermal camera is similar to the pinhole camera model of a conventional camera. The transformation from an object point $\mathbf{X}(X, Y, Z)$ to a local camera coordinate $\mathbf{x}(x, y)$ is:

$$x = \frac{\begin{array}{l} r_{11} \cdot (X - X_0) \\ +r_{21} \cdot (Y - Y_0) + r_{31} \cdot (Z - Z_0) \end{array}}{\begin{array}{l} r_{13} \cdot (X - X_0) \\ +r_{23} \cdot (Y - Y_0) + r_{33} \cdot (Z - Z_0) \end{array}}$$

$$y = \frac{\begin{array}{l} r_{12} \cdot (X - X_0) \\ +r_{22} \cdot (Y - Y_0) + r_{32} \cdot (Z - Z_0) \end{array}}{\begin{array}{l} r_{13} \cdot (X - X_0) \\ +r_{23} \cdot (Y - Y_0) + r_{33} \cdot (Z - Z_0) \end{array}} \quad (2)$$

where

$\mathbf{X_0}$	Projection centre
$r_{r,c}$	Elements of a rotation matrix $\mathbf{R}$

The coordinates projected into camera's coordinate system (origin at the camera projection centre; z-axis points toward the viewing direction; x-axis points to the right; y-axis points down) are further corrected for imaging errors caused by radial and tangential distortion effects. Lens distortion is modeled by a frequently used polysonomial model (BROWN 1971):

$$\begin{aligned} x' &= x(1 + k_1 r^2 + k_2 r^4 + k_3 r^6 \\ &\quad + p_2(r^2 + 2x^2) + 2p_1 xy) \\ y' &= y(1 + k_1 r^2 + k_2 r^4 + k_3 r^6 \\ &\quad + p_1(r^2 + 2y^2) + 2p_2 xy) \end{aligned} \quad (3)$$

where

$\mathbf{x}'$	Image coordinate free of distortions
$k_{[1;3]}$	Radial distortion coefficient
$p_{1,2}$	Decentering distortion coefficient
$r = \sqrt{x^2 + y^2}$	Radial distance

Finally, the projected point coordinates (u, v) in the image coordinate system (origin at top left image pixel; u-axis points to the right; v-axis points down) are calculated by shifting the coordinate system from the principal point to the origin of the image coordinate system, scaling in both image coordinate directions by focal length and correcting for skewness of the image axes:

$$\begin{aligned} u &= u_0 + x' c_u + y' s_1 \\ v &= v_0 + y' c_v \end{aligned} \quad (4)$$

where

$c_{u,v}$	Focal length in u and v image coordinate direction
u_0, v_0	Principal point
s_1	Coefficien describing the skewness of the two image axes

To reduce efforts in time and instrumental resources, photogrammetric self-calibration is favoured. In our application, geometric stability was assured in the self-calibrating bundle adjustment approach by jointly adjusting the low-resolution thermal image coordinate measurements with observations made in much higher resolution images captured by a DSLR Nikon D700. This requires the design of an adequate reference fiel with targets sufficientl visible in both the RGB and the thermal imagery.

Several strategies are reported in literature to deal with the problem of making reference points visible in thermal images: BISON et al. (2012) drilled holes in an aluminum surface. YASTIKLI & GULER (2013) designed a complex iron 3D test object, equipped with plastic targets. In LAGÜELA et al. (2011a), small lamps were arranged in a grid on a wooden plank. LUHMANN et al. (2013) applied this approach and utilized target lamps, too. They

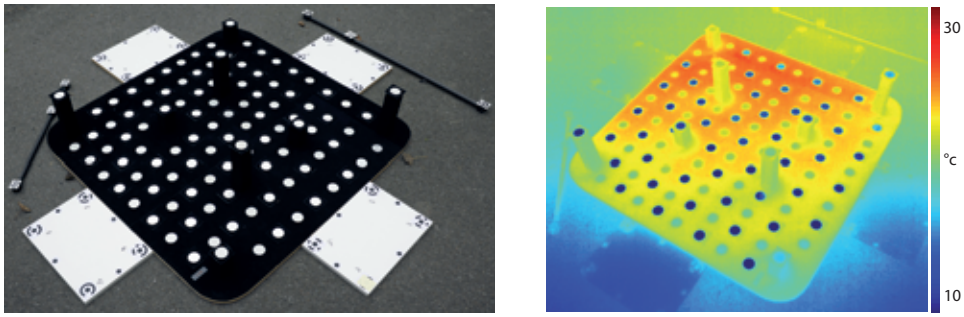

(a) (b)

Fig. 2: (a) True colour image and (b) colour-coded thermal image of a 3D target field.

Tab. 1: Thermal camera calibration parameters $\hat{x}_i$ with their standard deviations $\hat{s}_{\hat{x}_i}$. The image coordinate system is defined in section 3. The camera's pixel size is 17 µm, the camera's sensor size is 640 pixel × 512 pixel.

	c_u (px)	c_v (px)	u_0 (px)	v_0 (px)	k_1	k_2	k_3	p_1	p_2	s_1(px)
$\hat{x}_i$	774.65	774.46	315.75	259.57	-4.51e^{-2}	0.36	0	7.82e^{-4}	-1.13e^{-3}	6.37e^{-2}
$\hat{s}_{\hat{x}_i}$	0.197	0.202	0.267	0.254	1.36e^{-3}	9.80e^{-3}	fi	1.04e^{-4}	1.28e^{-4}	3.52e^{-2}

also reported about good experience with a metal reference fiel plate which reflect the cold background radiation well. The actual targets were made of self-adhesive foil which only emits radiation relating to its own temperature.

The 3D calibration plate designed for this work is also based on two material components: Silver heat protection foil with excellent reflectin properties for circular measuring marks is combined with black velour foil with good absorbing characteristics for target edging. In combination, both components provide a strong contrast in visible and infrared spectrum (Fig. 2). The centre coordinates of the circular targets (⌀40 mm) can be measured by an ellipse fit The mean standard deviation of the image point coordinate measurements was 1/40 of a pixel. These observations as well as additional scale information (reference bars) and approximate values for the unknown interior orientation parameters are introduced into a bundle adjustment procedure. Parameters were excluded from the bundle adjustment if they turned out to be insignifican in the significanc test. Outliers in the results were removed in an outlier detection procedure following 3-sigma rule.

Tab. 1 lists the interior orientation parameters and the corresponding a-posteriori standard deviations. All parameters could be determined significantl , except for the radial distortion parameter k_3. Regarding the precision of image point measurement stated above as well as the precision of the estimated geometric calibration parameters show that the calibration plate designed in combination with standard convergent imaging configuration is particularly suitable for thermographic camera calibration. The interior orientation thus estimated is used for 3D scene triangulation and dense 3D reconstruction (section 5).

4 Data Acquisition

The courtyard of an old urban building complex served as the test object in our study (Fig. 3a). The UAV introduced in section 6.2 was used to fl a raster pattern to capture thermal images of the entire surrounding façades (Fig. 3b). The façades are approximately 20 m in height and up to 50 m in length. Overall, more than 15,000 thermal images were acquired at 3 Hz with 90 % forward and 70 % side lap (Fig. 3c).

(a) (b) (c)

Fig. 3: (a) Aerial image of the subject of investigation. (b) Flying robot collecting data in front of a building façade. (c) Some of the thermal images.

The coordinates of 20 signalised circular targets, evenly distributed across one façade, were measured with a geodetic total station theodolite (TST) in order to provide a ground truth for evaluating the results (section 6). The design of those reference points is similar to the design shown in section 3, but the targets are larger, having a diameter of 140 mm. Following the law of error propagation for TST measurements, the RMSE of the resulting 3D coordinates can be estimated to be 4 mm. If TST coordinate differences are used as additional scaling distance information, the relative accuracy can be stated to be 2 mm. The corresponding image point coordinates of the centres are measured in thermal images by ellipse fi with a mean standard deviation of 1/30 of a pixel.

A terrestrial laser scanning point cloud acquired with a Riegl LMS-Z420i (3 million points, ca. 800 pts/m^2) is also used as a reference to analyze the quality of the point cloud obtained from the thermal images (section 6). The RMSE of a 3D point in TLS data depends on several influencin factors such as incidence angle, surface material or inaccuracies in registration and is given with about 10 mm in the dataset at hand (SCHNEIDER & MAAS 2007).

5 Data Processing and Results

The main goal of the work presented here is to reconstruct camera poses and 3D scene geometry purely from overlapping thermal imagery by using structure from motion (SfM) processing methods.

SfM techniques (e. g. FURUKAWA & PONCE 2007, MAYER 2008) generate 3D representations from 2D image sequences without initial information. Feature points are extracted from the images and matched, employing robust estimation techniques such as RANSAC (random sample consensus; FISCHLER & BOLLES 1981). This set of homologous points is then used to orient the images in a sequential bundle adjustment. Once interior and exterior orientations are calculated, dense image matching method such as semi global matching (SGM; HIRSCHMÜLLER 2005) can be employed.

The 14 bit signal of the thermal imaging sensor encodes temperatures in a range of –40 °C to +160 °C (sections 6.2 and 3). The environmental temperature during the measurement phase was +10 °C to +30 °C. In order to improve contrast for a reliable feature matching, the range of each image was expanded in a preprocessing step by histogram normalization. At the same time, the image depth was reduced to 8 bit in order to comply the image input formats required by the SfM tools used.

Image orientation was determined by VisualSFM, an integrated, open source SfM software package (WU 2011). Firstly, the SIFT operator detects and describes local feature points in the images (scale-invariant feature transform; LOWE 1999, WU 2007). The SIFT keypoints are, secondly, matched to identify homologous points between two images in a pair-wise image matching procedure. These correspondences are the basis for a bundle adjustment with robust outlier detection. It iteratively builds a sparse 3D model of the scene and simultane-

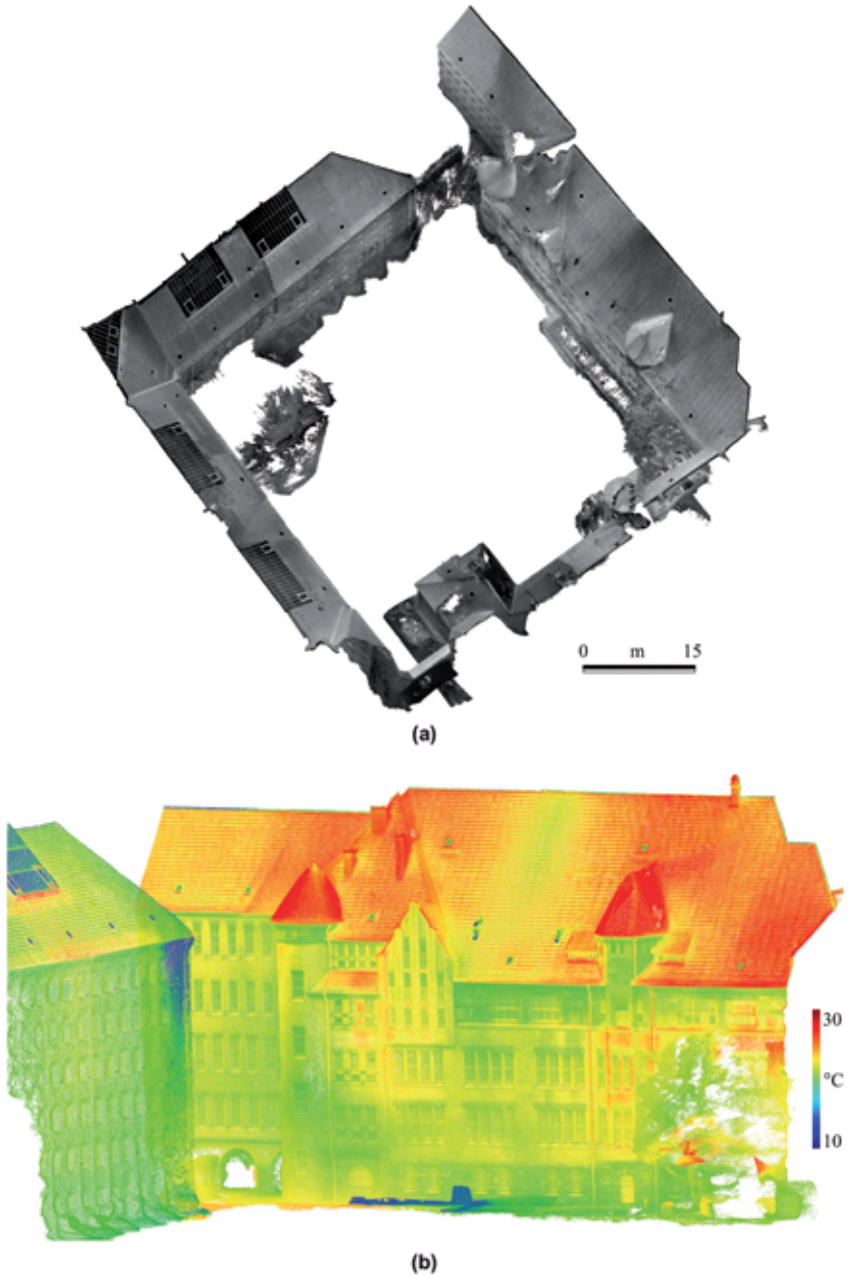

Fig. 4: 3D point cloud reconstructed from thermal images only: (a) Top view of the entire 3D model. (b) Temperature coded submodel of one façade.

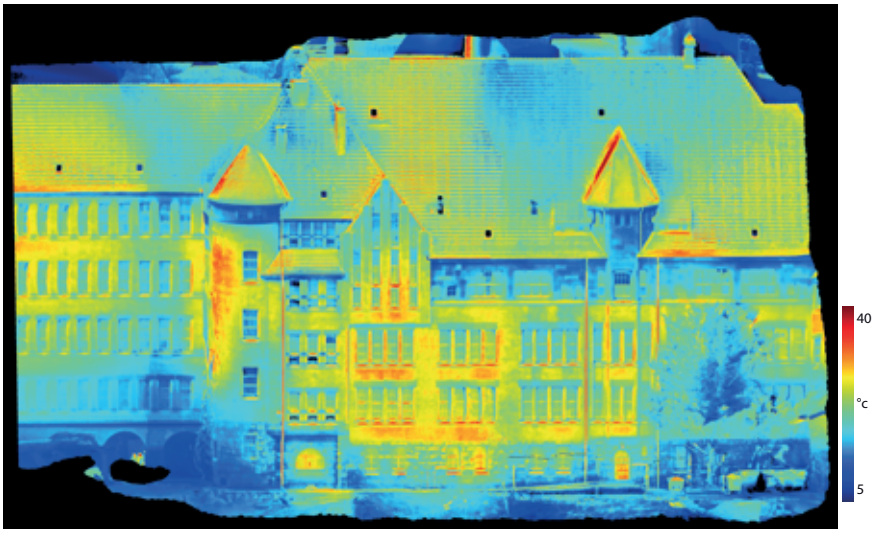

Fig. 5: TIR-attributed ortho-image of a part of one façade.

ously estimates the exterior orientations of all images; the interior orientation were kept constant, using the parameters derived as described in section 3. VisualSFM allows to produce multiple 3D models to reconstruct the entire scene, which is a particularly fl xible functionality for complex objects like the courtyard observed in this study. The internal camera model of VisualSFM includes only one radial distortion parameter. In order to consider the fully parametrized camera calibration model as described in section 3, the image coordinates of all homologous points as well as the camera orientations were imported into the commercial software package Agisoft PhotoScan. The camera calibration was fi ed to the parameters listed in Tab. 1, and another bundle adjustment was performed. In the next processing step, dense point clouds were derived from the given set of images and their orientation parameters by the dense image matching technique implemented in Agisoft PhotoScan.

The histogram stretching applied above must finall be reversed in order to provide thermal attributes. Each 3D point is re-projected into all corresponding image spaces where its temperature value is interpolated in a resampling process, weighted in accordance to the distance to the principal point.

The resulting 3D models can be scaled and geo-referenced either by using the tachymetric observations of the signalised control points or by aligning them to the previously acquired TLS dataset (section 4). In this study, an iterative closest point algorithm (ICP) minimizes the distance from the thermal point cloud calculated by structure from motion (as source) to the TLS point cloud (as reference) by iteratively applying a 3D Helmert transformation. The fina result consists of about 12 million TIR-attributed 3D points and is shown in Fig. 4.

Finally, ortho-rectifie façade images can be generated (Fig. 5). Orthographic projections of the building façades enable thermographic professionals to measure true distances directly in the image.

6 Accuracy Analyses

As the focus of the work presented here is on the accuracy potential of thermal cameras in 3D point cloud generation through SfM, several tests were performed to assess the accuracy. These tests include internal precision measures for image point measurements, camera poses and 3D object points (section 6.1) as well as external accuracy measures to validate the geo-

metric quality of the data using TST and TLS data as reference (sections 6.2 and 6.3).

The coordinate system of each submodel is oriented in a way that the façade forms the YZ-plane and the X-axis is oriented in camera's direction of view.

6.1 *SfM Internal Precision*

The SfM software tools used in this study (VisualSFM and Agisoft PhotoScan) deliver only very sparse information on the internal precision. Therefore, the SfM project data obtained after sparse reconstruction were fed into our own bundle adjustment software for a thorough accuracy assessment. The bundle adjustment delivers information on the precisions of the measured observations as well as the unknown camera poses and 3D object coordinates. In order to evaluate the pure results obtained from SfM tools, no further blunder checks were implemented. In the following, those results are presented.

The 2D coordinates of valid SIFT keypoints were introduced as a first group of observations. A second group contained the image point measurements of the signalised reference points. A variance component estimation (VCE; KOCH 2004) was used to ensure the adequate weighting of the two types of observations. The distances between the tachymetric observations of the signalised control points served as reference to scale the scene. The resulting additional constraint equations were weighted by a static variance component in accordance with the relative accuracy specification of a TST measurement given in section 4. The interior camera geometry was fixed to the parameters estimated in section 3. The exterior camera orientation parameters as well as the 3D coordinates of the object points calculated during SfM sparse reconstruction were treated as unknowns.

Tab. 2: A-posteriori standard deviations $\hat{s}_{\hat{x}_i}$ and mean point error $\hat{s}_{\hat{X}\hat{Y}\hat{Z}}$ of a 3D object point coordinates from a sparse point cloud in (mm). Row 1 and 3 are the mean, row 2 and 4 the median.

	$\hat{s}_{\hat{X}}$	$\hat{s}_{\hat{Y}}$	$\hat{s}_{\hat{Z}}$	$\hat{s}_{\hat{X}\hat{Y}\hat{Z}}$
SIFT	204.75	53.84	45.64	216.58
	160.40	34.19	32.22	167.14
Ref.	22.87	7.30	8.77	25.56
	23.12	6.19	8.82	25.50

The a-posteriori standard deviation $\hat{s}_{xy}$ of the original SIFT keypoints automatically adjusted by VCE was 1.1 pixel. This lack of subpixel accuracy corresponds to investigations on SIFT descriptors given in literature: REMONDINO (2006) states that with region detectors like SIFT the number of matched correspondences is quite high but the accuracy is poor, probably caused by perspective effects. The a-posteriori standard deviation $\hat{s}_{xy}$ of the signalised targets used as reference points is 1/3 of a pixel, and is thus significantly worse than the precision of the best-fit ellipses stated above. Reasons for that could be a too optimistic internal precision measure of ellipse-fitting. Furthermore, the size of the individual VCE observation groups is not well-balanced, to the disadvantage of the reference measurements (1:60). Self-calibration did not lead to any improvements in the estimated precision.

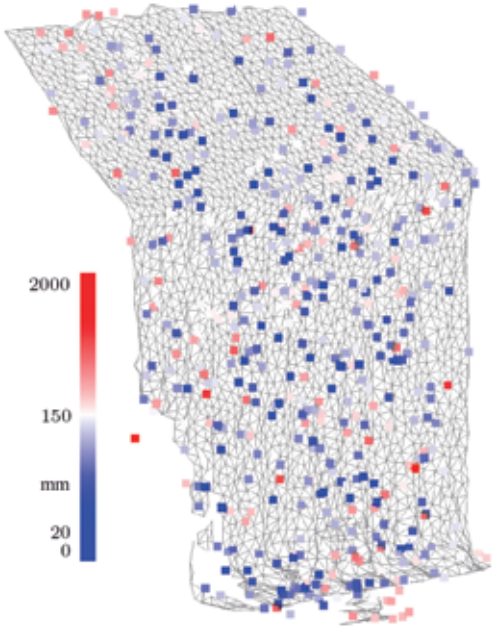

Fig. 6: 3D mesh of a part of the TLS reference façade, overlaid with colour-coded, logarithmically scaled mean point error of all 3D object points from sparse point cloud ranging from 20 mm to 1.8 m

Tab. 3: Mean a-posteriori standard deviations $\hat{s}_{\hat{x}_i}$ of camera's projection centres in (mm) and rotation angles in (°).

$\hat{s}_{\hat{X}_0}$	$\hat{s}_{\hat{Y}_0}$	$\hat{s}_{\hat{Z}_0}$	$\hat{s}_{\hat{X}_0\hat{Y}_0\hat{Z}_0}$
46.25	132.04	139.12	197.30

$\hat{s}_{\hat{\omega}}$	$\hat{s}_{\hat{\varphi}}$	$\hat{s}_{\hat{\kappa}}$
1.495	0.151	1.501

Tab. 4: Single 3D point precision in mm.

	$RMSE_X$	$RMSE_Y$	$RMSE_Z$	$RMSE_{XYZ}$
Intersection	18.28	4.45	4.92	19.45
Point picking	17.13	15.59	17.97	29.32

On an average, the a-posteriori standard deviations of the unknown 3D object coordinates $\mathbf{X}$ is 50 mm in planimetry and 200 mm in depth for all object points originating from SIFT keypoint observations (Tab. 2, row 1). The average a-posteriori standard deviation of the 3D object coordinates of the reference targets is 25 mm (Tab. 2, row 3). The accuracy for 3D SIFT points looks very high at a firs glance; however, it should be noted that this represents an average for all 3D points, including problematic regions such as edges or vegetation as well as points affected by a poor intersection geometry. As one can also see from Fig. 6, the depth precision of most of the façade points is between 20 mm to 100 mm. A more detailed evaluation of the single 3D point accuracy potential achieved after dense reconstructionis given in sections 6.2 and 6.3.

The a-posteriori standard deviations $\hat{s}_i$ of the unknown exterior orientation parameters are in average 200 mm for camera positions $\mathbf{X_0}$ and 1.0° for camera rotations $\omega\varphi\kappa$ (Tab. 3). Due to correlations between several camera orientation parameters, the internal precision figure of the projection centres are worse than the 3D point precision achieved above, an effect which is also known from aerial photogrammetry. The lower precision in roll (ω) and yaw (κ) can be explained by a partly fragmentary cross overlap in image configuratio for this part of the court yard.

6.2 *External 3D Point Accuracy*

For an external accuracy test, the 3D coordinates of the 20 reference target points were calculated by spatial intersection, using the measured image coordinates and the camera orientation parameters as determined in section 5. These 3D object coordinates were compared with the TST reference coordinates. The residual discrepancies after a 3D Helmert transformation between the two datasets are listed in Tab. 4, row 1. The RMSE of a 3D object coordinate $\mathbf{X}$ is about 20 mm.

The 3D coordinates of the reference points can also be measured directly in the dense point cloud. Due to sampling errors, they actually do not match exactly with the true centres of the circular reference targets. This is reflecte in a too pessimistic RMSE in lateral direction, but the RMSE in depth direction (here X) is comparable to its equivalent determined by spatial intersection for points on a planar façade (Tab. 4, row 2).

The façades were captured with a ground sampling distance (GSD) of 26 mm for an average measurement distance of 20 m. Thus, the RMSE in depth direction is 2/3 of the GSD, which is a very promising ratio for 3D model reconstruction from low resolution thermal images and well comparable to the accuracy obtained for digital surface models automatically created from aerial images (HIRSCHMÜLLER & BUCHER 2010).

6.3 *Comparison of SfM and TLS Point Clouds*

The deviations between the SfM dense point cloud and the TLS reference point cloud are shown in Fig. 7, using a colour code for visualisation. For each point of the SfM point cloud,

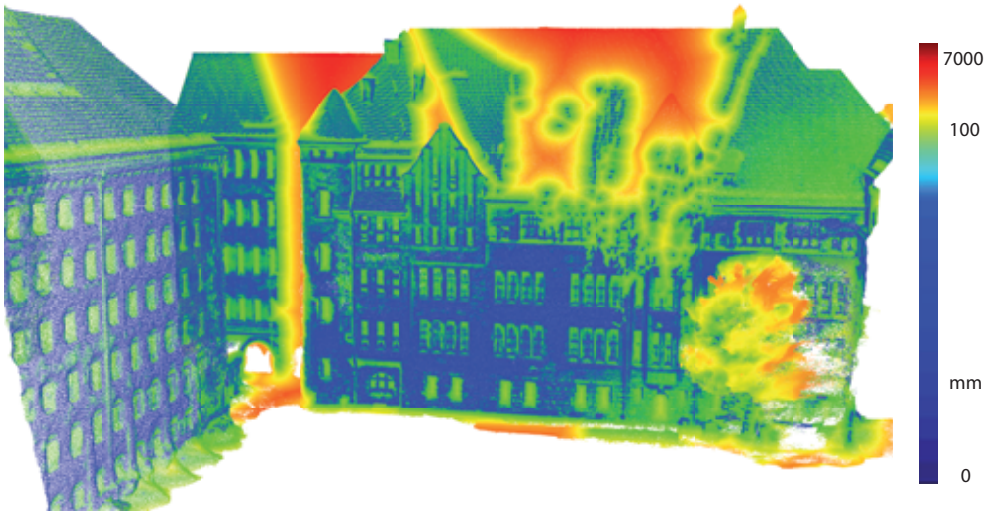

Fig. 7: Colour-coded, logarithmically scaled differences between SfM and TLS point clouds.

the Euclidean distance to the nearest point in the TLS point cloud was computed (nearest neighbour distance). Ignoring TLS blind spots caused by occlusions in the TLS dataset as well as vegetation (yellow, orange and red areas), the deviations are less than 25 mm in average for façade structures (roof areas as well as window areas reflectin TIR-radiation were excluded), obtained from a total of 12 million 3D points. The accuracy value contains the actual measurement error of SfM coordinates as well as the representation error from the sampling process.

6.4 *Discussion*

These external precision figure obtained from a comparison of the 3D point cloud as a result from dense matching with data acquired by terrestrial laser scanning constitute a rather rigorous accuracy check – and they are surprisingly good, considering the fact that it is purely based on data of a thermal camera with small sensor format as well as specifi contrast and texture conditions. The results obtained from signalised reference points (section 6.2) confir these figures Surprisingly, the internal precision figure obtained from processing the "black box" SfM project data with our own bundle adjustment are much worse. This can be explained by the fact that the SfM project data were not filtere and that the dataset also contained points in occluded areas and on vegetation, which were excluded in the analysis in section 6.3. Moreover, it should be noted that the matching tools used to produce the sparse data in section 6.1 (SIFT) and the dense representation tested in section 6.2 (dense image matching) were different, with the SIFT operator delivering a high robustness, but a lower image measurement precision.

7 Conclusion

The work presented here deals with reconstructing TIR-attributed 3D building façades purely from UAV-based thermal images. Structure from motion techniques are used to estimate camera orientations and 3D object point coordinates without any initial information. The results are very promising: The façades of a courtyard of a building complex could completely be represented by a dense 3D point cloud consisting of about 12 million points. The RMSE of the TIR-attributed 3D points was found to be less than 20 mm in a comparison with terrestrial laser scanner data, the depth accuracy is about 2/3 of the ground sampling distance.

Future work should concentrate on the radiometric resampling process. The data quality may be improved by considering the 3D object geometry in the resampling and correction of thermal attributes. The radiometric accuracy potential should also be investigated.

Acknowledgements

The research work presented in this paper has been funded by the European Social Fund (ESF) via Sächsische Aufbaubank (SAB). We would also like to thank our partners in the ADFEX project for their support and the great collaboration.

References

BANNEHR, L., SCHMIDT, A., PIECHEL, J. & LUHMANN, T., 2013: Extracting Urban Parameters of the City of Oldenburg from Hyperspectral, Thermal, and Airborne Laser Scanning Data. – PFG - Photogrammetrie, Fernerkundung, Geoinformation **2013** (4): 367–379.

BISON, P., BORTOLIN, A., CADELANO, G., FERRARINI, G., FURLAN, K. & GRINZATO, E., 2012: Geometrical correction and photogrammetric approach in thermographic inspection of buildings. – 11th International Conference on Quantitative InfraRed Thermography: http://www.ndt.net/article/qirt2012/papers/QIRT-2012-285.pdf (3.8.2015).

BROWN, D.C., 1971: Close-range camera calibration. – Photogrammetric Engineering **37** (8): 855–866.

DERENIAK, E.L. & BOREMAN, G.D., 1996: Infrared detectors and systems. – 1. edn., Wiley-Interscience: ISBN-13 978-0471122098.

FISCHLER, M.A. & BOLLES, R.C., 1981: Random sample consensus: A paradigm for model fittin with applications to image analysis and automated cartography. – Communications of the ACM **24** (6): 381–395.

FLIR, 2012: User documentation, FLIR A6xx series. – FLIR Commercial Systems. Meer, Belgium.

FURUKAWA, Y. & PONCE, J., 2007: Accurate, dense, and robust multi-view stereopsis. – IEEE Conference on Computer Vision and Pattern Recognition 2007 (CVPR '07): 1–8.

GONZÁLEZ-AGUILERA, D., RODRIGUEZ-GONZALVEZ, P., ARMESTO, J. & LAGÜELA, S., 2012: Novel approach to 3D thermography and energy efficien y evaluation. – Energy and Buildings **54**: 436–443.

HARTLEY, R.I. & ZISSERMAN, A., 2004: Multiple View Geometry in Computer Vision. – Second edn., Cambridge University Press, ISBN:0521540518, United Kingdom.

HIRSCHMÜLLER, H., 2005: Accurate and effi cient stereo processing by semi-global matching and mutual information. – IEEE Computer Society Conference on Computer Vision and Pattern Recognition, 2005 (CVPR 2005), Volume 2: 807–814.

HIRSCHMÜLLER, H. & BUCHER, T., 2010: Evaluation of digital surface models by semi-global matching. – DGPF Tagungsband **19** (2010): 571–580.

HOEGNER, L., KUMKE, H., MENG, L. & STILLA, U., 2007: Automatic extraction of textures from infrared image sequences and database integration for 3D building models. – PFG – Photogrammetrie-Fernerkundung-Geoinformation **2007** (6): 459–468.

HOEGNER, L., WEINMANN, M., JUTZI, B., HINZ, S. & STILLA, U., 2013: Co-registration of time-of-fligh (ToF) camera generated 3D point clouds and thermal infrared images (IR). – SEYFERT, H. (ed): DGPF Tagungsband, Dreilndertagung DGPF, OVG, SGPF, Volume **22**, 481–488.

HOEGNER, L. & STILLA, U., 2015: Building facade object detection from terrestrial thermal infrared image sequences combining different views. – ISPRS Annals of Photogrammetry, Remote Sensing and Spatial Information Sciences **II-3/W4**: 55–62.

IWASZCZUK, D., HOEGNER, L., SCHMITT, M. & STILLA, U., 2012: Line based matching of uncertain 3d building models with IR image sequences for precise texture extraction. – PFG – Photogrammetrie, Fernerkundung, Geoinformation **2012** (5): 511–521.

KLIX, M., SCHNITZER, F., PFANNE, M. & JANSCHEK, K., 2014: Guidance-Navigation-Control System zur 3D-Exploration von ausgedehnten Objekten mit Multi-Roboter-Systemen. – 63. Deutscher Luft- und Raumfahrtkongress (DLRK), Augsburg: on CD-ROM.

KOCH, K.-R., 2004: Parameterschätzung und Hypothesentests in linearen Modellen. – 4. edn., Ferd. Dümmler Verlag, Bonn.

KOHLER, S., AGRICOLA, A.-C., JOEST, S., PETERS, S. & STOLTE, C., 2013: Energieeffizien als Säule der Energiewende. – Energiewirtschaftliche Tagesfragen **63**: 8ff.

LAGÜELA, S., GONZALEZ-JORGE, H., ARMESTO, J. & ARIAS, P., 2011a: Calibration and verificatio of thermographic cameras for geometric measurements. – Infrared Physics & Technology **54** (2): 92–99.

LAGÜELA, S., MARTÍNEZ, J., ARMESTO, J. & ARIAS, P., 2011b: Energy efficien y studies through 3D laser scanning and thermo-

graphic technologies. – Energy and Buildings **43** (6): 1216–1221.

LOWE, D.G., 1999: Object recognition from local scale-invariant features. – Seventh IEEE International Conference on Computer Vision, Volume **2**: 1150–1157.

LUHMANN, T., PIECHEL, J. & ROELFS, T., 2013: Geometric calibration of thermographic cameras. – Thermal Infrared Remote Sensing: 27–42, Springer.

LUHMANN, T., ROBSON, S., KYLE, S. & HARLEY, I., 2006: Close Range Photogrammetry: Principles, Methods and Applications. – Revised edn., Whittles Publishing, Dunbeath, United Kingdom.

MAURIELLO, M.L. & FROEHLICH, J.E., 2014: Towards automated thermal profilin of buildings at scale using unmannedaerial vehicles and 3D-reconstruction. – 2014 ACM International Joint Conference on Pervasive and Ubiquitous Computing: Adjunct Publication, UbiComp '14 Adjunct. ACM: 119–122, New York, NY, USA.

MAYER, H., 2008: Issues for image matching in structure from motion. – International Archives of Photogrammetry, Remote Sensing and Spatial Information Sciences **37** (B3a): 21–26.

PECH, K., STELLING, N., KARRASCH, P. & MAAS, H., 2013: Generation of multitemporal thermal orthophotos from UAV data. – ISPRS-International Archives of the Photogrammetry, Remote Sensing and Spatial Information Sciences **1** (2): 305–310.

REMONDINO, F., 2006: Detectors and descriptors for photogrammetric applications. – The international archives of the photogrammetry, remote sensing and spatial information sciences **36** (3): 49–54.

RUDOL, P. & DOHERTY, P., 2008: Human body detection and geolocalization for uav search and rescue missions using color and thermal imagery. – Aerospace Conference, 2008 IEEE: 1–8.

SCHNEIDER, D. & MAAS, H.-G., 2007: Integrated bundle adjustment of terrestrial laser scanner data and image data with variance component estimation. – The Photogrammetric Journal of Finland **20**: 5–15.

WU, C., 2007: SiftGPU: A GPU implementation of Scale Invaraint Feature Transform (SIFT): http://cs.unc.edu/ccwu/siftgpu/ (3.8.2015).

WU, C., 2011: VisualSFM: A Visual Structure from Motion System: http://ccwu.me/vsfm/ (3.8.2015).

YASTIKLI, N. & GULER, E., 2013: Performance evaluation of thermographic cameras for photogrammetric documentation of historical buildings. – Boletim de Ciéncias Geodésicas **19** (4): 711–728.

Addresses of the Authors:

Dr. PATRICK WESTFELD, DAVID MADER & Prof. Dr. HANS-GERD MAAS Technische Universität Dresden, Institute of Photogrammetry and Remote Sensing, D-01062 Dresden, e-mail: {patrick.westfeld}{david.mader} {hans-gerd.maas}@tu-dresden.de

Manuskript eingereicht: Mai 2015
Angenommen: August 2015

PFG 2015 / 5, 0395–0410
Stuttgart, October 2015

Report

High Resolution Land Cover/Land Use Mapping of Large Areas – Current Status and Upcoming Trends

Klaus-Ulrich Komp, Münster

Keywords: land use, land cover, monitoring, advanced methodologies, validation

Summary: Land use, land cover, and their dynamics are of high relevance for geographic research and increasingly interesting for many administrative, economic and environmental institutions. During the past four decades remote sensing from satellite images has been an emerging technology which allowed for the observation of the Earth's surface even in remote parts of the world. Starting in the field of global meteorological and climatic dynamics, observations expanded to vegetation monitoring, which in turn can specifically support research and development in the field of food production. This report from science and technology highlights the methodological challenge for extracting land use classes from land cover types, the technological progress since the 1970s and recent applications on European and global levels.

The report introduces two different publicly available regional and global land cover maps as well as land cover monitoring datasets. It reports on their significance of class definition, spatial resolution and thematic focus. Recent high resolution global datasets are evaluated according to their methodological progress and their potential for further applications. Finally, the upcoming trends in high resolution global mapping and monitoring are presented.

The focus is not only on scientific progress but also on changing information demand, as needs from different fields of application will help to generate the necessary funds for the improvement of methods. The overall benefit will be a better knowledge of the actual dynamic of the world regarding food resources and environment.

Zusammenfassung: *Hochauflösende großräumige Kartierung von Bodenbedeckung und Bodennutzung – Aktueller Status und sich abzeichnende Trends.* Bodenbedeckung und Landnutzung und ihre Veränderung sind nicht nur für die geographische Forschung von großem Interesse sondern auch für den wachsenden Informationsbedarf vieler administrativer, wirtschaftlicher und umweltrelevanter Institutionen. Seit vier Jahrzehnten hat sich die Fernerkundung mit Satellitenbildern als Technologie etabliert, um auch die entferntesten Regionen der Welt zu beobachten. Beginnend mit der Beobachtung globaler meteorologischer und klimatischer Veränderungen entwickelte sich die Vegetationsbeobachtung mit ihren präzisen Beiträgen zur Nahrungsmittelproduktion als Forschungs- und Entwicklungsfeld. Der Beitrag beleuchtet die methodische Herausforderung, unterschiedliche Landnutzungen aus Klassen der Bodenbedeckung abzuleiten, sowie die technologischen Fortschritte seit den 1970er Jahren und die aktuellen Anwendungen auf europäischer und globaler Ebene.

Der Beitrag stellt verschiedene regionale und globale öffentlich zugängliche Datensätze der Bodenbedeckungskartierung und Landnutzungsveränderungsentwicklung vor. Er untersucht die Signifikanz der Klasseneinteilung, der räumlichen Auflösung und der thematischen Ausrichtung soweit zutreffend. Aktuelle Ergebnisse hochauflösender regionaler und globaler Datensätze werden hinsichtlich ihres methodischen Fortschritts und ihres Potenzials für zukünftige Anwendungen evaluiert. Schließlich werden die sich abzeichnenden Trends regionaler und globaler Kartierung und Veränderungsbeobachtung vorgestellt. Der Fokus liegt dabei nicht nur auf dem wissenschaftlichen Fortschritt, sondern auch auf dem sich wandelnden Informationsbedarf, weil die Anforderungen verschiedener Anwendungsfelder dazu beitragen werden, die notwendigen Mittel für den methodischen Fortschritt zu generieren. Der Gesamtnutzen wird sich durch eine bessere Kenntniss der Weltdynamik hinsichtlich Resourcen und Umwelt darstellen.

www.schweizerbart.de
DOI: 10.1127/pfg/2015/0276
1432-8364/15/0276 $ 4.00

1 Introduction

Beginning with the start of the first Earth Resource Satellite missions in the early 1970s there have been many attempts to obtain global overviews on land use and land cover, vegetation, settlements and natural resources. While the first satellite capacities could not easily provide a real global data coverage in short time periods among others due to revisit limitations, several modern satellite systems today offer such opportunities like more frequent observations at high geometric resolutions. The readily available image data now allows for more precise evaluation of limits and potentials of thematic land mapping and the respective maps showing the land use, the land cover, or the vegetation status and development.

There is a very strong demand for determining and monitoring the land use on all scales. Remote sensing has been perceived as a solution to overcome the unbalanced updating of cartographic maps (Konecny 2013). Not only for scientific but especially for environmental and economic reasons information on land use and land use development are required. For instance, the actual land use and the potential for land use development together with crucial questions of land ownership are amongst the prime determining factors in socio-economic and investment decisions.

However, satellite images predominantly offer information on land cover and can hardly supply such specific information demand. In the early global and continental remote sensing products of low and medium resolution, this challenge was not obvious. Some investigations show that this gap between potentials and demands was already recognized early (Anderson et al. 1976), but the new potential of remote mapping was frequently overestimated. With improved data resolutions and a more detailed differentiation of land use classes, the problem of ambiguities between land cover and land use has become more apparent. For instance, the land cover "grassland" may result from different land use types, such as a meadow within the land use "agriculture", a lawn within the land use "public recreation", a soccer turf within the land use "sport field" or even a grass field within the land use "airport". These problems have been tackled either by local validation or by attempts of automatic semantic and geometric interoperability. In those approaches, the difficulty of applying regional mapping solutions to large area applications became evident. In addition, the variety of ecological, hydrological and sub surface conditions demand regional adaptions of classification methods for mapping extensive areas.

In this paper, the forthcoming trends will be examined not only on the basis of their scientific and technical aspects, but also with respect to their societal, administrative and economic aspects.

2 Large Area Land Cover

To understand the different approaches, it is worth looking at large scale land cover mapping projects. There, study areas cover entire countries or continents and remote sensing has to be performed without or with only reduced access to ground truth information for training and validation. From 1974 until 1977, the United States Department of Agriculture (USDA), NASA and NOAA conducted the first phase of the Large Area Crop Inventory Experiment (LACIE). The experiment was designed to develop a monitoring method targeted on wheat production in important agricultural regions throughout the world (U.S., Canada, USSR, and Brazil). The technological basis was the image data received since 1972 by the Earth Resource Technology Satellite (ERTS), later renamed Landsat-1. The project achieved proving the usefulness of multispectral image data to extract timely crop information with a strong focus on wheat (Erb & Moore 1979). This initial concentration on a single-class classification of multispectral data as well as the political support and significance contributed to its success: As a result it became possible for the United States to predict the wheat harvest for extensive wheat production regions in the Soviet Union several weeks prior to harvest within a relatively small margin of error. Yield predictions rely not merely on the determination of crop extend and acreage, but also on crop conditions, which are highly influenced by the spatio-tem-

poral variability of temperature and precipitation. This explains why the researchers of the LACIE project used additional meteorological data to refine their results (NASA 1978).

2.1 *Pan-European Approach of CORINE*

In 1985, the European Commission initiated the project "Coordination of Information on Environment" (CORINE), a very ambitious programme to monitor a great number of environmental features and their spatial distribution and development. In the end, the only feature which was successfully realised was land cover, because the methods by remote sensing from orbital platforms available at this time could not resolve high levels of detail required for more specific land use mapping. Most of the other important environmental features could not be implemented due to unresolved scientific and administrative discussions about definitions and observation techniques on a European scale. When the first CORINE Land Cover (CLC) started, it was based on the reference year 1990 and on Landsat 5 data. Initially the inventory was designed with a minimum mapping unit (MMU) of 25 ha and 44 land cover classes. For the subsequent updates, the Landsat 7 and SPOT data were included, and the MMU of changes was reduced to 5 ha (Figs. 1 and 2).

After the European Environment Agency (EEA) became operational in 1994 in Copenhagen, tasks within the Directorate General Environment were assigned step by step to the EEA, including the CLC 2000 update. Later on the CLC time series were embedded in the structural context of the programme "Global Monitoring for Environment and Security" (GMES). From 2012 onwards, after GMES had been renamed to Copernicus, the CLC time series became part of this programme, too. Where member states are using national digital landscape models updated with satellite image data such as the DLM-DE (Basic Digital Landscape Model for Germany, see section 4.2), the CLC updates will no longer be performed separately, but will be derived from these landscape models.

Working experiences through more than two decades of CLC mapping have shown the specific challenges of large area cover approaches. There are several land cover classes which do not occur in certain regions or which will have different ecological relevance e.g. according to site-specific edaphic conditions. Comparing the different European member-states discloses a certain variability of ecological zones and agro-climatic conditions. For accurate mapping within these zones different seasonal windows for acquiring satellite image data are useful. As the national land cover classes have developed independently in most cases, the CLC approach has to be recognised as a successful attempt to harmonise the European land cover map on an unbiased basis of Earth observation methodology.

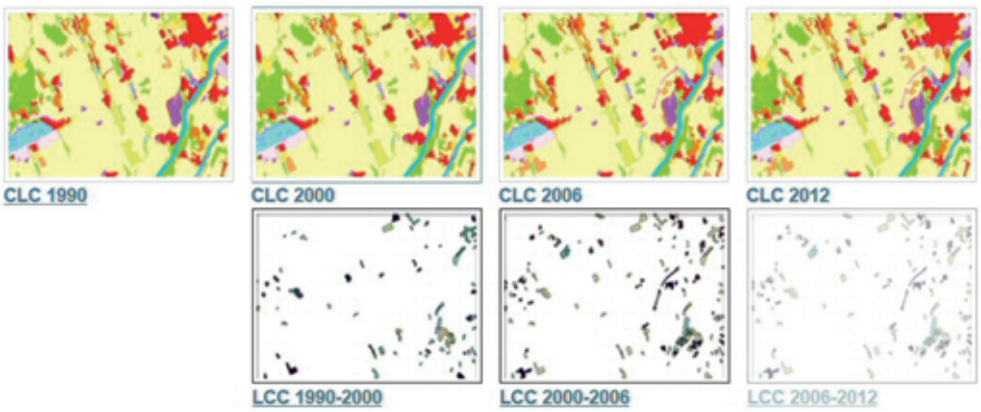

Fig. 1: Monitoring stages of CORINE Land Cover (Copernicus 2014).

Fig. 2: CORINE Land Cover 2006 main classes (COPERNICUS 2014).

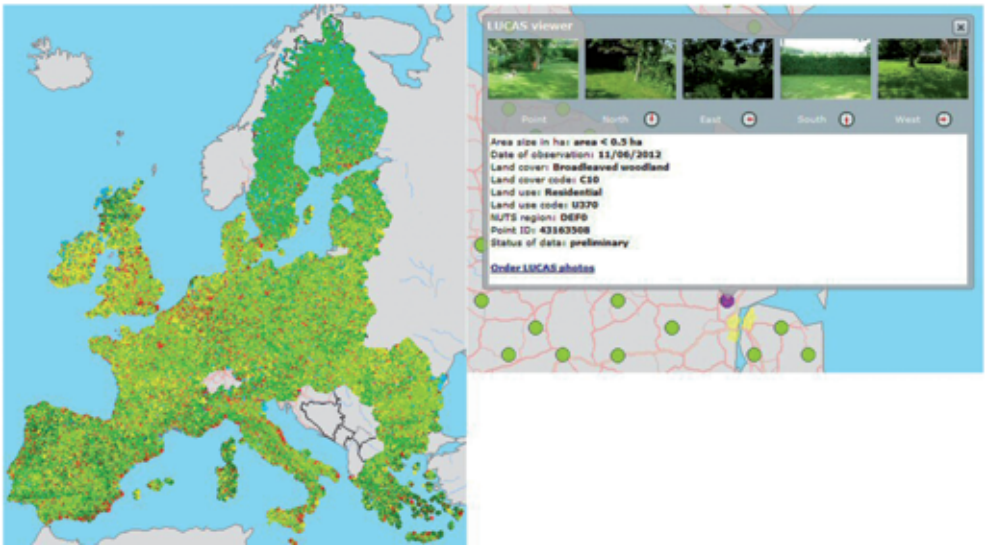

Fig. 3: LUCAS 2012 survey results: Overview of land cover sample points main classes (left); Example LUCAS terrain sample survey and photos (right) (COPERNICUS 2014).

2.2 *LUCAS – the European Sample Monitoring Approach*

In 2001 surveys throughout the European member states were started which have been conducted approximately every three years. The latest update (2015) consists of another 270,000 points observed in a sample survey of land cover classes, actual land use, soil conditions, and ecological features including a photo documentation of about 1.5 million terrain witness photos. Based on a stratified sampling in a 2 km by 2 km grid, the database of EUROSTAT (2015) offers a unique pool of land use/land cover samplings on the ground. Fig. 3 shows an overview of the 2012 survey results depicting the main land cover classes.

The right part of Fig. 3 shows an example of the terrain photos. The first image in the series shows the sample point itself and the other four depict the neighbourhood of the sample point in cardinal directions. Over the last 15 years, the LUCAS database has been a unique source of information on the spatial development of land cover change throughout Europe, a big dataset showing the relation between land cover and land use, as well as an on-site view collection which could provide a valuable calibration source for further refinement of remote sensing classifications.

3 Global Approaches

The early approaches for a global coverage were often limited by capacity constraints of the few existing satellites and by frequent cloud cover in many parts of the world. Therefore, the first global satellite maps often needed more than five years to achieve a complete coverage. More recently several satellite constellations are providing image data with a ground sampling distance (GSD) between 30 m and 5 m at short repeat cycles. Methodologically, the global view has highlighted additional problems arising from the different climatic zones and the different seasonal characteristics between the tropic zone, the Northern and the Southern hemispheres. Hence the global approaches of Earth observation had to incorporate various ecological patterns and a regional adapted scheme of object catalogues. As a general rule it can be stated that the need for regional adaption is growing with the reduction of the MMU.

3.1 *Copernicus Global*

In 1988, the European Commission initiated a joint programme with the European Space Agency (ESA) called “Global Monitoring of Environment and Security”, better known under its acronym GMES. Under this umbrella a great number of initiatives, projects, and service elements were developed. Three examples of this programme’s output are A) the service element of “Global Monitoring for Food Security” (GMFS) with regional components directed towards Africa (Brockmann et al. 2011, Komp & Haub 2012, Haub et al. 2013), B) the Fast Track Service “Land” under the Framework Programme FP7 of the European Commission within the GMES initiative, and C) a bundle of Geoland 2 projects, like the African Area Frame Sampling in the course of the SATChMo projects. Parallel to those R&D projects, the European Commission initiated direct global monitoring themes, predominantly focussing on biophysical parameters like climate and vegetation. Copernicus, previously known as GMES, is the European Programme for the establishment of a European capacity for Earth observation. The different projects, results and reports are now accessible through the Copernicus Land Monitoring Services of the European Commission (Copernicus 2014).

One attempt at global monitoring within this framework was the Global Land Cover Project initiated by the Joint Research Centre (JRC) of the European Commission. This venture started under the umbrella of a project entitled as Global Environment Information System (GEIS). The task was to “provide information on changes in the world’s vegetation cover for EU policy in the area of environment, development and external affairs” (Bartholomé et al. 2002). The Vegetation instrument on board of the SPOT 4 satellite offered a quick but coarse coverage. A cooperation of about 30 research groups developed a common legend for the GLC 2000 product, using the “Land Cover Classification System”

(LCCS) terminology concerted between JRC and United Nations Food and Agriculture Organisation (FAO) (Fig. 4).

Simultaneously, similar attempts were conducted by the FAO. The current product is called "Global Land Cover – SHARE" (GLC-SHARE) and was launched as a beta release in March 2014. The database utilises the ISO standard LCCS to harmonize various land cover databases of land cover products from all over the world (Fig. 5). The improved LCCS has been used as basis for the "Land Cover Meta Language" (LCML), which is able to specify any land cover type around the world according to detailedness and scale. By using LCML, the researchers were able to create 11 global land cover classes in accordance with to the System of Environmental Economic Accounting (SEEA).

The database is geometrically compiled within a pixel resolution of 30 arc-seconds, corresponding to ~1 km × ~1 km. The area south of latitude 60° S was not included in the data base. While Northern America, Eu-

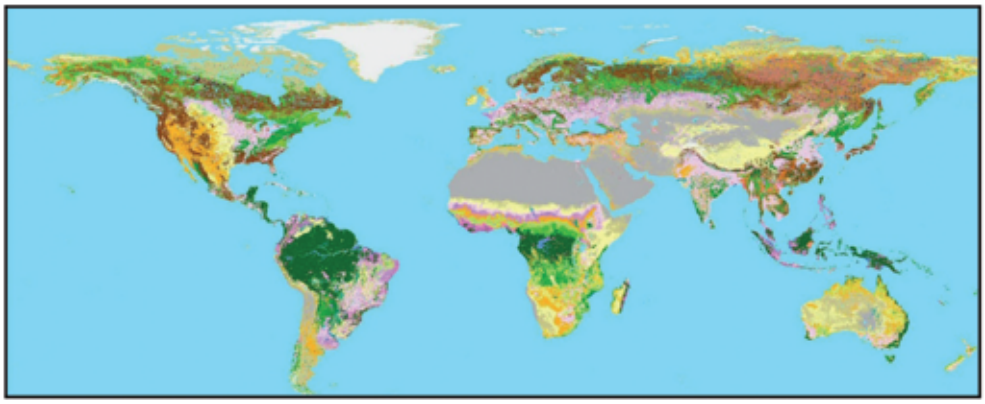

Fig. 4: Global Land Cover2000 Product (Bartholomé et al. 2002).

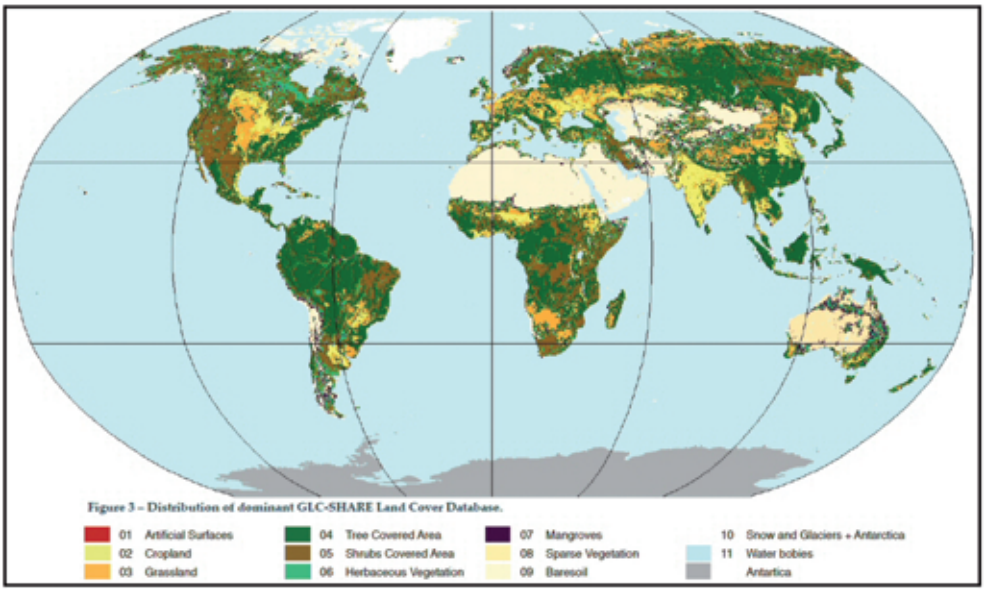

Fig. 5: GLC SHARE Land Cover Data Base Map (Latham et al. 2014).

Tab. 1: CLC-SHARE 2014 Quality Assessment (own compilation from Latham et al. 2014).

GLC-SHARE Land Cover Types	Label	Global fraction	User's accuracy	Producer's accuracy
Artificial Surfaces	01	0,6 %	70,0 %	100,0 %
Cropland	02	12,6 %	94,9 %	88,8 %
Grassland	03	13,0 %	75,4 %	65,6 %
Tree covered Areas	04	27,7 %	94,9 %	91,8 %
Shrub covered Areas	05	9,5 %	50,0 %	67,9 %
Herbaceus vegetation	06	1,3 %	56,0 %	53,8 %
Mangroves	07	0,1 %	80,0 %	100,0 %
Sparse vegetation	08	7,7 %	50,0 %	44,3 %
Baresoil	09	15,2 %	57,3 %	89,6 %
Snow and glaciers	10	9,7 %	96,3 %	72,2 %
Water bodies	11	2,6 %	100,0 %	66,7%
Total		100,0 %		

rope, the Eastern half of Africa, Russia, China, some Southern Asian states, and Australia were covered by high resolution datasets, Southern America, the Western half of Africa, the Arabian Peninsula, India, and the Indonesian Archipelago were only covered by global datasets of coarse resolution.

Nearly 1,000 sampling sites were included using a stratified random design in order to perform a validation of CLC-SHARE 2014. The result of the accuracy assessment is shown in Tab. 1. The overall accuracy has been calculated to be 80.2 %. FAO is expecting that the reliability will increase with updates which may use improved databases.

3.2 *GLC Global Land 30*

Between 2010 and 2013, the Chinese National Geomatics Center (NASG) prepared two global land cover maps with a resolution of 30 m for the reference years 2000 and 2010 from freely available Landsat scenes. The initiative was launched as a national 30 m GLC mapping project. It was listed as a GEO subtask SB-02 C1 (Chen 2013).

To obtain a dataset for the reference year 2000, the National Geomatics Centre of China in Beijing processed 10,270 Landsat TM scenes. For the update 2010, they included 2,640 scenes from the Chinese HJ-1 satellite together with 9,907 Landsat TM datasets. For four years, around 500 scientists worked on the geo-coding and thematic processing of this data and developed a variety of sampling techniques, classification and change detection procedures, e.g. the spectral gradient difference (SGD) based approach for land cover change detection (Chen et al. 2013). The GLC30 product comprises 10 land cover classes (Fig. 6).

For the scientific user community it is very important that the complete data base for both reference years including sample areas and reference data like CORINE are available as a web service (GLC30 2015). About 139 map sheets have been independently validated in sample areas by five international research groups, confirming a disagreement generally lower than 5%.

3.3 *Need for Validation*

All of the aforementioned land cover products face the same fundamental problem: The lower the number of ground samples, the more the automated classification approaches have to extrapolate land cover characteristics into

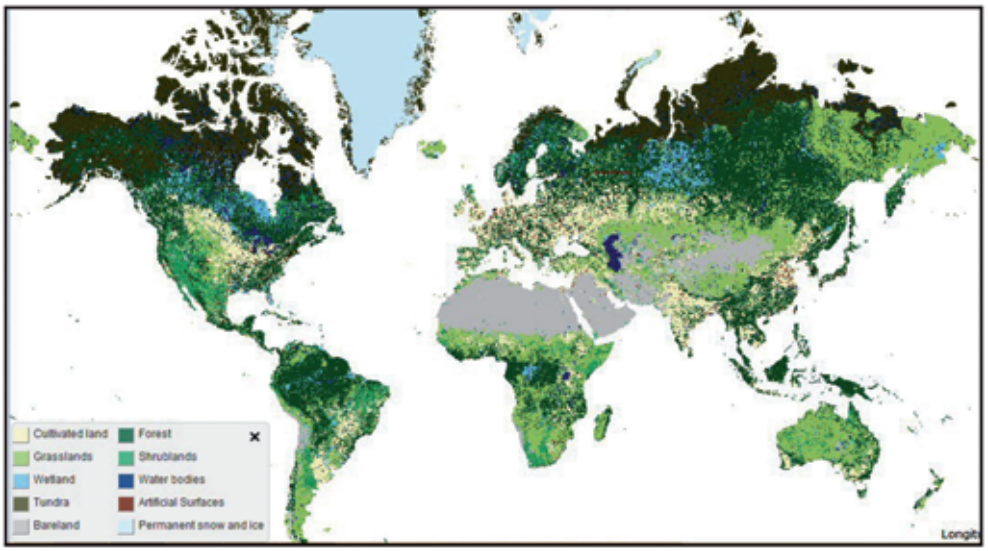

Fig. 6: GLC Global Land 30 result for 2010 (GLC30 2015).

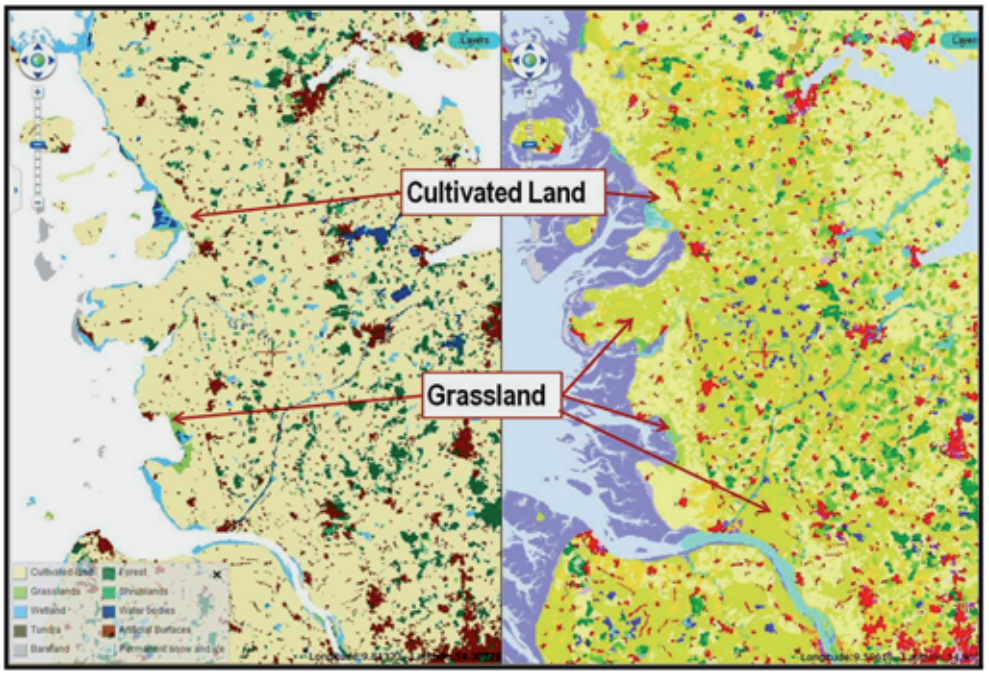

Fig. 7: Validation of GLC Global Land 30 (2010) against CORINE (CLC) at the example of North-West Schleswig-Holstein in Northern Germany (GLC30 2015).

unsampled regions, which in turn increases the risk of misclassification. However, world coverage will hardly be completed without a certain margin of uncertainty inherent to time saving automation.

Fig. 7 shows the comparative view of an extract from the GLC30 and the corresponding CLC 2006 of a small part of Northern Germany between the city of Hamburg in the lower right corner and the German-Danish border of about 16,500 km^2, separating the North Sea (West) from the Baltic Sea (East). Artificial surface, water bodies, and forest show a very good compliance. However, the GLC30 maps differ from the CLC map in a strip of 40 km width and 120 km length parallel to the Western coast, where the CLC maps shows predominantly grassland (CLC code 231). At least in this area, this will result to an underestimation of grassland cover to the benefit of the cultivated land ratio. Some other differences in the tidal flats along the North Sea coast are not of great importance as in the global view, these tidal amphibious lands are in the range of Mangrove coasts extensions, which also are not subject of GLC30. This example may underline the potentials for further improvements of the reference database as part of the next update of GLC30, which has already been announced in Chen (2013).

In order to cross-check the assumption of the CLC map being a valid data base, the results from the Copernicus project, funded under the FP7 scheme, were consulted. There are results available from a temporal analysis of a representative part of Schleswig-Holstein, which are shown in Fig. 8 in the development from 1990 to 2001 to 2013. The source for the

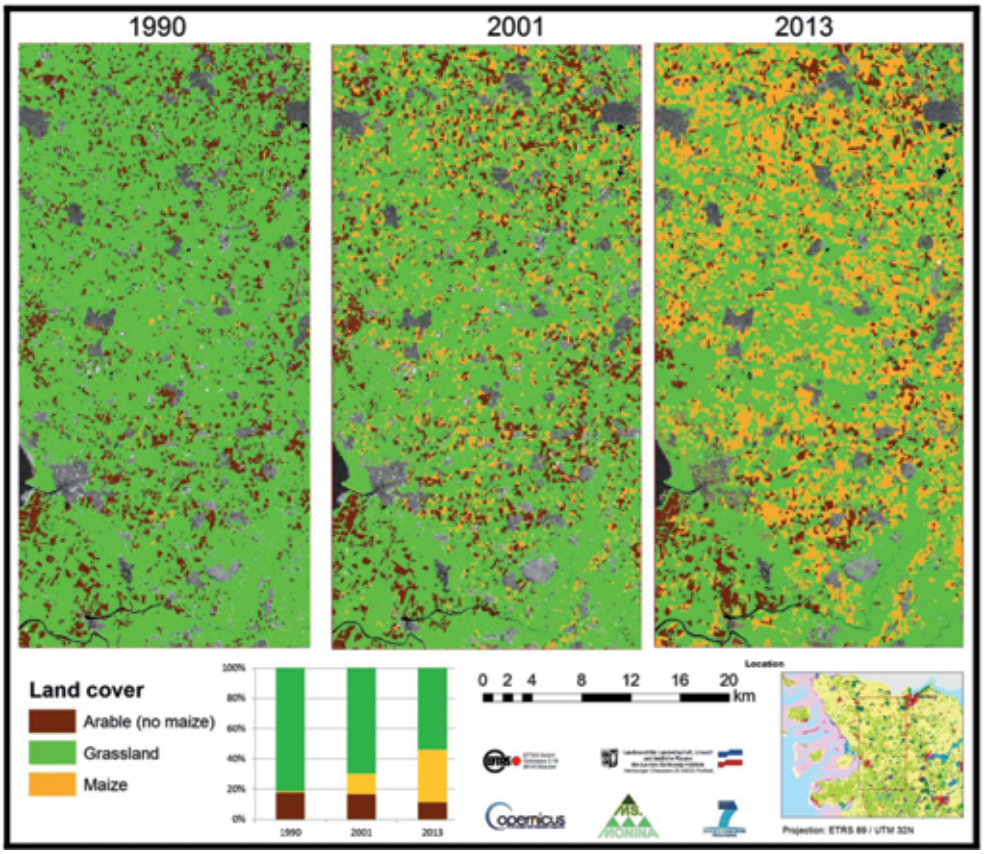

Fig. 8: Dynamics of agricultural changes in the validation area for Schleswig-Holstein in Northern Germany through conversion of grassland into bio-fuel production area with maize (adapted from Buck et al. 2013, Buck et al. 2015, and MS.MONINA 2013).

map of 2013 was satellite data from Landsat 8, acquired on 2013-05-02, 2013-06-03 and 2013-07-21. The base classification from 1990 and 2001 were used from the state BNTK data base (Survey of Biotope and Land Use Types), which has also used SPOT5 data. Using recent satellite image data from 2013, agricultural changes were classified. A conversion of grassland to arable land (cultivated cropland) could be identified and compared to existing previous classifications (Buck et al. 2013, Buck et al. 2015). Due to its edaphic conditions grassland habitats dominate the region. In 1990, there had still been a predominant exploitation of grassland. The statistical distribution diagram below the three maps shows about 81% of grassland for 1990 and only few maize cropping. Around 2001, a considerable conversion of grassland began for the biomass production through planting maize. In 2013, the proportion of grassland was found reduced (55%) at the expense of maize area (35%). This shows that different from the GLC30 in 2010 with mainly cropland in this area, there was still about 55% of grassland left even in 2013 (Figs. 7 and 8). The latter is being monitored by the regional Ministry of Agriculture as these biofuel production areas are in the vicinity of Natura 2000 sites.

4 Monitoring Land Cover / Land Use Changes

4.1 *Methodological Challenge to bridge the Gap between Land Cover and Land Use*

Spatial patterns on the surface of the Earth are of special socio-economic interest in terms of their actual use or the potential to change the actual use by different actors. The value of usable parts of the Earth's surface is determined by natural properties of the land or by access to the land and increases with competing human interests. Land offers potential for food production, cattle husbandry, settlement, economic production, circulation, recreation and extraction of Earth resources. Therefore, the knowledge of the land use is an important parameter in decisions concerning most human activities, especially with regard to a growing world population on a limited Earth surface. This also applies to militant annexation of foreign land as well as the present globalisation of trade and exchange. Many stakeholders, regional planners and investors require to know about the land use more or less worldwide.

The principal gap between required land use and observed land cover manifests in different parameters and their values. Generally spoken, the size of the gap grows with reduced pixel size and with increasing number of land use classes. In the initial ERTS-1 pixel size of 80 m × 80 m most natural or urban surfaces appeared rather interpolated and therefore appropriate to pixel based classification techniques of that time. Today's high-resolution satellite data, ranging from 10 m to 5 m is more difficult to classify due to many small differentiations, height differences, shadows and variations in illumination. In high resolution images there are less areas of homogeneous appearance than in image data of medium resolution. The problem naturally increases when using very high resolution image data (<5 m).

The second reason for a gap between required land use and observed land cover is the number of land use classes. The CORINE Land Cover describes land cover and land use according to a nomenclature of 44 classes organised hierarchically in three levels. The first level comprises four classes, the second level 15 classes, and the third level 44 classes. Especially in the latter case spectral confusion occurs in particular when one land cover type can refer to several land use classes. As a consequence, there have been a series of different approaches tested during the last decades to refine automatic land cover classification by introducing algorithms for calibration, interpretation keys gained from field observation, libraries of spectral characteristics (reference signatures), knowledge based training parcels and object based class similarities.

4.2 *Methodological Advances in DeCOVER*

In the course of a R&D project for space-based services for German land cover, the DLR initiated the development of approaches to over-

come the gap between land cover and land use. The project DeCOVER focussed on the existing international and national land cover models like CORINE land cover, ATKIS Basis-DLM (Authorative Topographic-Cartographic Information System – Basic Digital Landscape Model), and DLM-DE with the aim of also supporting the future of the European land service components within Copernicus. Methodologically, different services had to be addressed: The automatic detection and classification of land cover changes, agricultural monitoring, environmental monitoring, and the crucial question of overcoming the partial discrepancies between the different existing national and international land cover models.

This special research field needs to be explained in detail. Satellite based land cover data is supposed to have an area fully covered by a number of land cover classes, without overlaps and without any unclassified gaps between adjacent areas. Contrary to this, the ATKIS Basis DLM provides information on land cover and land use, normally with several layers of information (cadastre, legal requirements, land use, built-up structures, public limitations on real estate use, economic zoning, etc). The project has improved approaches to semantic and geometric interoperability in order to derive object classes from different cadastre objects, comparable based on a common vocabulary as shown in Fig. 9 (Christ & Lessing 2012, DeCOVER 2013). A method was developed that allows semantic translations for many classes. For some classes even a geometric translation between the remote sensing derived land cover and the administrative and legal land use became possible. For now, these are R&D results achieved within the realm of knowledge-based regional context. To further develop this method into a reliable service element, i.e. a method transferable to other areas, additional experience-based case applications are still required. The fast spread satellite based monitoring of large areas at high resolution will be limited by not enough regional knowledge bases of the same standards. Potentially, the 15 years of recurrent LUCAS surveys can help to extend the knowledge base of land use and land cover, at least in Europe.

These recent developments of methodological advances combined with repeatedly updated sample surveys give a very good perspective on improving the possibilities for large area land cover/land use monitoring based on ubiquitously available high-resolution satellite data.

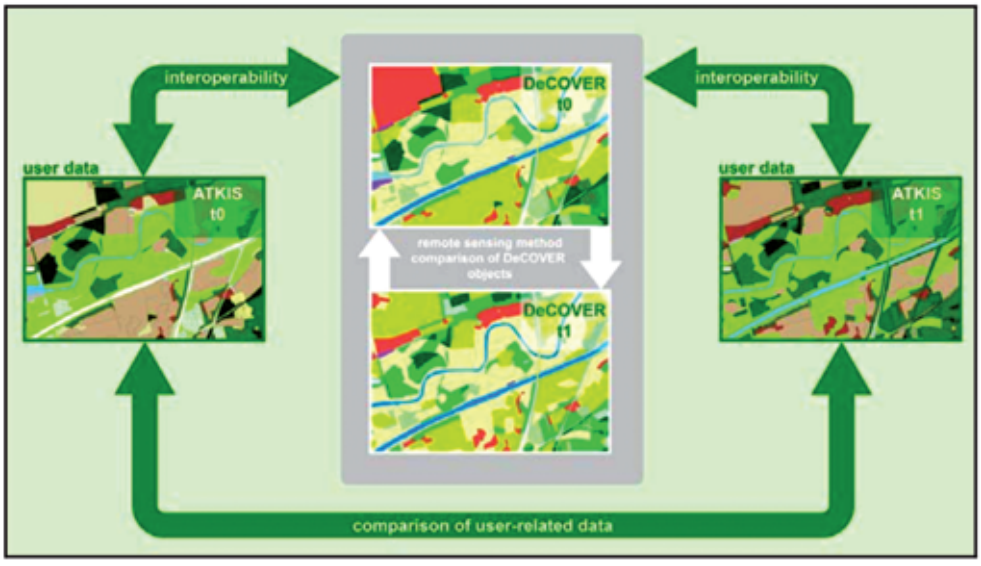

Fig. 9: Knowledge based semantic and geometric interoperability (DeCOVER 2013).

5 Upcoming Trends in Large Area Monitoring

Several trends that can be observed of late will strengthen further advances in high-resolution large scale land cover products. One important issue is the continuation of high-resolution satellite programmes, even as a combination of satellite resources from different providers. It is very promising that there is not only the Landsat continuity. Also the upcoming Sentinel series, the RapidEye constellation, Spot 7, ResourceSat-2 of India and the Chinese HJ-1 have already been enlarging the observation capacity (Tab. 2). Further follow-up satellites are either already under construction or planned.

A second supporting field emerges from various projects and international initiatives: Originated as a project only, the "Global Observation of Forest Cover – Global Observation of Land Dynamics" (GOFC_GOLD) has now become an initiative working actively for several years to promote and improve global Earth observation. The Committee on Earth Observation Satellites (CEOS), the Group of Earth Observation (GEO), the United Nations (often through FAO), and many regional or national governmental institutions are pushing Earth observation into a confluence of methodological and technical progress (Mora et al. 2014).

Fortunately, there is another trend with a growing driving force, though sometimes not in the focus of the scientific communities. This support comes from an emerging group of users of global land cover information. The first global information of coarse resolution has created rising interest for information of better geometric and temporal resolution. The traditional user group has different administrative interests, like disaster mitigation, support to regional planning and zoning, monitoring of water resource regions, desertification, climate, biodiversity, ecosystem conservation and vegetation characteristics and change (Mora et al. 2014). Additionally, there is a special demand among the governmental user group to apply Earth observation for supporting information collection and mapping in developing countries and less-favoured regions (Komp et al. 2010, Völker et al. 2011). The ongoing globalization of all social and economic relations has created a third important support group: the private sector, meaning the society as a whole. Besides the scientific interest of all Earth-related disciplines, there is increasing interest in free access to global land cover information from private persons for travel, foreign investments, social engagement of NGOs

Tab. 2: Specification of existing and upcoming satellites for high resolution EO mapping (selection compiled from information of the different satellite operators).

Satellite	GSD	Bands	Repeat Cycle	Operation
RapidEye constellation	5 m	5 MS	1 day (5 satellites)	since 2.2009
HJ-1A/HJ-1B	30 m	4 MS	4 days (2 satellites)	since 1.4.2009
Resource Sat-2	6 m LISS-4 / 30 m LISS-3	3 MS / 4 MS	24 days	since 28.4.2011
Landsat 8	30 m MS / 15 m pan	9 MS / 1 pan / 2 mw	16 days	since 11.2.2013
Sentinel 1A	5 m x 5 m strip map mode	1 C-SAR	12 days	since 3.4.2014
Spot 7	6 m / 1.5 m	4 MS /1 pan	26 days	since 30.6.2014
Sentinel 2A	10 m / 20 m / 60 m	4 MS / 6 MS / 3 mw	10 days	since 22.6.2015
Sentinel 1B	5 m x 5 m strip map mode	1 C-SAR	6 days (2 satellites)	planned for 2016
Sentinel 2B	10 m / 20 m / 60 m	4 MS / 6 MS / 3 mw	5 days (2 satellites)	planned for 2016
EnMAP	30 m	250 hyperspectral	21 days	planned for 2018

and various economic activities. It has to be pointed out, that apparently free Internet access to data for navigation, maps, aerial views and street views does not mean that this data has been created and provided free of charge. Those charges are covered by a global, powerful advertising industry which will refinance these costs through increasing sales and profit, which in turn will result in tax income of the concerned states. Globally these applications of "free" spatial information for the purpose of navigation, travelling, and other social activities not only create a rising demand for actualized spatial data but also contribute via tax income to public research budgets.

Initially, the main profiting sectors are agriculture, forestry, mineral resources extraction, and the energy sector. All of these depend on knowing the spatial patterns in up-to-date, precise terms and often benefit significantly from land cover information. These stakeholders are prepared to finance projects that go beyond the free access of information, and generate information that is more specific. Such growing demand driven by globalisation will provide funding for scientific progress in Earth observation, even in times of declining budget resources.

The developments above will be the basis for the scientific-technical trends in high-resolution global land cover mapping. The ongoing changes are evident in user-oriented alterations of monitoring cycles, monitoring scales and monitoring subjects. In regions like the upper Amazonian forest or the North Siberian tundra, in the absence of governmental programmes, large scale mapping will only occur on demand.

Simultaneously, another trend is the increasing online access to all geographic data. The Chinese GLC30 data base already offers an online validation tool which may in future serve to broaden the sources for local input of knowledge ("crowd sourcing validation"). Furthermore, the number of people travelling for private or work related reasons will increase further and require more specific information on their destination via online access. Undoubtedly, this will produce new forms of displaying tailored land cover mapping with individual focus on specific user needs. This means that areas of economic, touristic or political interest will enjoy more frequent mapping and updates than other regions. Those regions with low or no interest will be left to the possibilities of public cartographic updates.

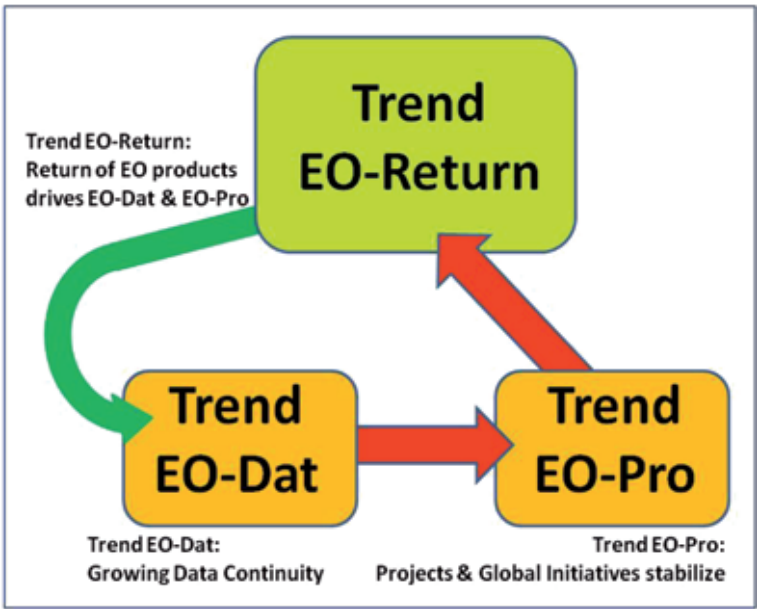

Fig. 10: Upcoming trends in Earth observation and their interaction.

The interaction of different upcoming trends in Earth observation is illustrated in Fig. 10. Based on the described developments, three major trends emerge, effectively shaping the next decade of Earth observation. The first trend may be labelled as "**Trend EO-Dat**". We observe that the data continuity is growing because of a rising number of satellite systems in orbit. As projects and global initiatives are stabilising in growth, they form the driving force which we label as "**Trend EO-Pro**". The GOFC-GOLD Initiative, CEOS, GEO, the United Nations, and the FAO are pushing EO into a confluence of methodological & technical progress. The third major development can be summarized as "**Trend EO-Return**". As pointed out above, we find many global application fields where products of Earth observation already produce an important economic and technical return on investments.

Economic sector studies have predicted solely for the European downstream market induced by the Copernicus EO programme additional 63,000 jobs until 2030, connected to a downstream market potential of 1.8 billion € (Space-Tec Partners 2012). 25 years ago the activities of Earth observation remained still in the shadow between photogrammetric mapping and scientific research depending only on public budget allocations. The example of car navigation systems may stand for the bigger investments done by the industrial sector to produce in a few years image and map coverages. Nobody did expect that Earth observation including the geo-information sector would become subject to merger and acquisition activities of global importance. The US company Planet Labs, founded 2010 in San Francisco, operates 28 small satellites and has acquired BlackBridge's RapidEye and geospatial businesses in mid 2015. The acquisition of SPOT Image by Astrium or the acquisition of HERE by the automotive industry are just two other examples. Once those EO products have reached a certain level of acceptance and distribution, user requirements will generate the need for further updates, better accuracy, and new product developments. However, the return of EO products has begun to drive the growth of the other trends EO-Dat and EO-Pro. The global trend "EO-Return" enjoys support by different user fields:

- Globalised users of global land cover monitoring who are discovering the social and economic return of EO,
- a global society (private sector) demanding free access to global land cover information,
- navigation and travel,
- social engagement of NGOs,
- the resource sector (Agriculture, Forestry, Minerals, Water) etc.

Growing demand will create user-oriented alterations of monitoring cycles, monitoring scales and monitoring subjects: Return from EO utilisation will finance and drive future R&D projects and monitoring demand.

6 Conclusion

Since the first satellite images have been available, global land cover mapping data has been the key source for researchers, governments and private users. At selected examples this report demonstrated the scientific developments and technological progress since the Large Area Crop Inventory Experiment through which the United States predicted wheat yield in the Soviet Union. Furthermore, different land cover datasets were discussed to highlight regional and global developments of land cover and land use mapping. In terms of high resolution and actuality, the Chinese Global Land Cover change detection dataset presently appears to have the highest standard. The GLC30 product shows a high quality of information content and web based functionalities, but also indicates potential for local improvement. The existing challenge of mapping land use within one land cover class remains a field for further research. The approaches of object-based classifications like the R&D results of the DeCOVER project have shown promising results. The semantic and geometric interoperability will need more regional sample definitions in order to allow the application in large scale Earth observation products.

The demand for ongoing large area land cover observation is expressed by different user communities. Upcoming trends comprise more data continuity with higher resolution, harmonisation and standardisation of mapping procedures, but also emerging user

demands and new user communities based around web services. In conclusion, these prospects will broaden a user community who perceives the Societal Benefit Areas (SBA) of Earth observation. In turn, this provides a common mandate for all researchers and experts involved to support the advancement of this field, as their engagement in EO and high-resolution land cover monitoring will contribute to a responsible and sustainable development of our planet Earth.

References

Anderson, J.R., Hardy, E.E., Roach, J.T. & Witmer, R.E., 1976: A land use and land cover classification system for use with remote sensor data. – Geological Survey Professional Paper 964, United States Government Printing Office, Washington DC, USA.

Bartholomé, E., Belward, A.S., Achard, F., Bartalev, S., Carmona-Moreno, C., Eva, H., Fritz, S., Grégoire, J.M., Mayaux, P. & Stibig, H.J., 2002: GLC 2000 Global Land Cover mapping for the year 2000. – European Commission, Joint Research Centre, EUR 20524 EN, 66 p., Ispra, Italy.

Brockmann, J., Haub, C. & Komp, K., 2011: Global Monitoring for Food Security Stage 3 (GMFS 3). – PFG – Photogrammetrie, Fernerkundung, Geoinformation **2011** (3): 194–195.

Buck, O., Klink, A., Garcia Millán, V., Pakzad, K. & Müterthies, A., 2013: Image analysis methods to monitor Natura 2000 habitats at regional scales – the MS-MONINA State Service Example in Schleswig-Holstein, Germany. – PFG – Photogrammetrie, Fernerkundung, Geoinformation **2013** (5): 415–426.

Buck, O., Garcia Millán, V., Klink, A. & Pakzad, K., 2015: Using information layers for mapping grassland habitat distribution at local to regional scales. – International Journal of Applied Earth Observation and Geoinformation **2015** (37): 83–89.

Christ, I. & Lessing, R., 2012: Semantische und geometrische Aspekte der Interoperabilität. – DGPF-Tagungsband **21:** 18–25.

Chen, J., Wu, H., Li, S., Liao, A., He, C. & Peng, S., 2013. Temporal logic and operation relations based knowledge representation for land cover change web services. – ISPRS Journal of Photogrammetry and Remote Sensing **83:** 140–150.

Chen, J., 2013: 30-m GLC map. – GEO-X Plenary, Towards International Collaboration on Global Land Cover Products and Services, 14.1.2013, Geneva, Switzerland.

Copernicus, 2014: Copernicus Land Monitoring Services. – www.land.copernicus.eu/pan-european/corine-land-cover (4.3.2015).

DeCOVER, 2013: DeCOVER 2 – Space based services for German land cover. – 12 p., www.decover.info (10.7.2013).

Erb, R.B. & Moore, B.H., 1979: The Large Area Crop Inventory Experiment /LACIE/ – A summary of three years experience. – 5th Canadian Symposium on Remote Sensing, August **1978:** 542–554, A79-36486 15-43,Victoria, BC, Canada.

EUROSTAT, 2015: LUCAS online viewer. – http://ec.europa.eu/eurostat/statistical-atlas/gis/viewer/?myConfig=LUCAS-2012.xml (2.3.2015).

GLC30, 2015: http://globallandcover.com/GLC30Download/index.aspx (14.8.2015).

Haub, C., Kleinewillinghöfer, L., Brockmann, J., Komp, K. & Gilliams, S., 2013: Monitoring Services for Food Security – Successful Transfer of Technology to the Sudanese Government. – PFG – Photogrammetrie, Fernerkundung, Geoinformation **2013** (5): 459–472.

Komp, K., Dienst, H. & Haub, C., 2010: Anwendungspotenziale der Erdfernerkundung für Entwicklungsländer. Erkenntnisse aus dem Technologietransfer – politische und gesellschaftliche Bedingungen für den Einsatz der Fernerkundung in Entwicklungsländern. – Gutachten im Auftrag des TAB (Büro für Technikfolgenabschätzung beim Deutschen Bundestag), Münster, verarbeitet in Fernerkundung: Anwendungspotenziale in Afrika **2012:** 57 p.

Komp, K. & Haub, C., 2012: Global Monitoring for Food Security and Sustainable Land Management – Recent Advances of Remote Sensing Applications to African and Siberian Show Cases. – International Archives of Photogrammetry, Remote Sensing and Spatial Information Sciences XXXIX-B8, **2012:** 265–270, Melbourne, Australia.

Konecny, G., 2013. The International Society for Photogrammetry and Remote Sensing (ISPRS) study on the status of mapping in the world. Global Geospatial Information. – International workshop of the Siberian State Academy of Geodesy and ISPRS: 4–24, Novosibirsk, Russia.

Latham, J., Cumani, R., Rosati, I. & Bloise, M., 2014: Global Land Cover SHARE (GLC-SHARE) database. – Beta-Release Version 1.0., FAO, Rome, Italy.

Mora, B., Tsendbazar, N.-E., Herold, M. & Arino, O., 2014: Global land cover mapping: current status and future trends. Land use and land over mapping in Europe: practices & trends. – Re-

mote Sensing and Digital Image Processing **18:** 11–30, Dordrecht, The Netherlands.

MS.MONINA, 2013: http://geoweb2.sbg.ac.at/ms_monina/doc/MS_MONINA_Del4_4_v10.pdf (15.8.2015).

NASA, 1978: LACIE – Phase I and phase II accuracy assessment final report. – http://www.nass.usda.gov/Education_and_Outreach/Reports,_Presentations_and_Conferences/GIS_Reports/Phase%20I%20and%20II%20Accuracy%20Assessment%20Final%20Report%20%28Pages%201-100%29.pdf (14.8.2015), Houston, TX, USA.

Space-Tec Partners, 2012: Copernicus GIO Lot3 – European Earth Observation and Copernicus Downstream Services Market Study. – Publishable Executive Summary, 17 p., Service Contract 89/PP/ENT/2011 – LOT 3.

Völker, A., Müterthies, A. & Hölzel, N., 2011: Implementation of a monitoring system for land cover changes in the Western Siberian corn-belt – A remote sensing approach from the SASCHA project. – Environment and Natural Resource Management **2011:** 233, Tyumen, Russia.

Address of the Author

Dr. Klaus U. Komp, EFTAS Remote Sensing Transfer of Technology, Oststrasse 2 – 18, D-48145 Muenster, Germany, Fax: +49-251-13307-33, e-mail: klaus.komp@eftas.com

Manuskript eingereicht: Juni 2015
Angenommen: August 2015

Berichte von Veranstaltungen

3rd International Workshop on Compressive Sensing Theory and its Applications to Radar, Sonar, and Remote Sensing (CoSeRa), 16. – 19. Juni 2015, Pisa, Italien

Der dritte internationale Workshop zu *Compressive Sensing Theory and its Applications to Radar, Sonar, and Remote Sensing* fand vom 16. bis zum 19. Juni 2015 in Pisa, Italien, statt. Die Hauptverantwortlichen für die Veranstaltung waren Fulvio Gini (Università di Pisa), Joachim Ender (Fraunhofer FHR), Maria Sabrina Greco (Università di Pisa) und Matthias Weiss (Fraunhofer FHR).

Insgesamt umfasste der Workshop ein Tutorial, drei Keynote-Vorträge, vier thematisch unterschiedlich ausgerichtete Oral Sessions und vier Poster Sessions. Die individuellen Blöcke fanden sequentiell statt, so dass alle Teilnehmer am gesamten Programm teilnehmen konnten. Der Workshop hatte das Ziel, Mathematiker und Ingenieure zusammenzubringen, die im Bereich Radar, Sonar und Remote Sensing arbeiten und in ihrer Arbeit Methoden des Compressive Sensing nutzen.

Zu den Keynote-Vorträgen waren namhafte Gastredner eingeladen. Moeness Amin (Villanova University, USA) referierte über *A Sparsity-Perspective to Time-Frequency Signal Representations*, Holger Rauhut (RWTH Aachen) gab in seinem Vortrag *Compressive Sensing in Radar – A Mathematical Overview* zunächst einen Überblick über die mathematischen Grundlagen von Compressive Sensing und ging im Folgenden auf die Anwendung des Schätzverfahrens im Bereich der Radar-Technik ein. Müjdat Cetin (Sabanci University, Türkei) ging in seinem Vortrag zu *Sparsity-Driven SAR Imaging: History, Computatio-*

Abb.: Kathedrale und Schiefer Turm von Pisa.

DOI: 10.1127/pfg/2015/0277 1432-8364/15/0277 $ 1.50

nal Advances, Learning, Other Forms of Simplicity unter anderem darauf ein, wie spärliche Signale zur Analyse von SAR-Szenen mit bewegten Objekten genutzt werden können.

Im Rahmen der Oral Sessions wurden insgesamt 25 Beiträge zu den Themen *Sparse sensing in synthetic aperture imaging systems*, *Signal recovery and detection*, *Sparse sensing application in radar* und *Compressive acquisition techniques* vorgestellt. Die vier Poster Sessions deckten die Themengebiete *Signal recovery and detection*, *Sparse sensing applications in radar*, *Compressive sensing in SAR, ISAR and Tomography* und *DoA estimation and array processing* ab. Die Poster waren strategisch günstig in der Nähe des Kaffeebuffets angebracht, so dass viele Teilnehmer die Zeit zum wissenschaftlichen Austausch und für intensive Diskussionen mit den jeweiligen Autoren nutzten.

Im Tutorial zum Thema *Compressive Covariance Sensing for Radar Applications* gab Geert Leus (TU Delft) einen Überblick über die Schätzung spektraler Leistungsdichten, z.B. Winkel- und Frequenzspektrum, über komprimierte Beobachtungen und hob die Unterschiede zu klassischen Compressive Sensing Anwendungen hervor. Denn in vielen ingenieurwissenschaftlichen Anwendungen ist nicht die Rekonstruktion eines kompletten Signals, sondern oft nur die Schätzung von Statistiken zweiter Ordnung nötig.

Von insgesamt 70 eingereichten vollständigen Beiträgen (Full Paper, 5 Seiten) wurden 58 (83%) angenommen und in Form von Vorträgen oder Postern präsentiert. Sie sollen in IEEEXplore veröffentlicht werden. Drei studentische Beiträge wurden mit dem *Best Student Paper Award* der CoSeRa ausgezeichnet.

Zusammenfassend ist festzuhalten, dass die Veranstaltung hervorragend organisiert war, wofür den Verantwortlichen und Helfern herzlich zu danken ist. Ebenso werden das ansprechende Ambiente während des Social Events rund um den Schiefen Turm von Pisa sowie die eindrucksvolle Luminara di San Ranieri vielen Teilnehmern sicher noch lange in guter Erinnerung bleiben.

Marion Heublein, Karlsruhe

Hochschulnachrichten

First Joint PhD Colloquium on Geoinformatics of DGK and DGPF

From February 16 to 17, 2015, the first joint PhD colloquium of the DGPF working group on geoinformatics and the DGK section for geoinformatics was held at the University of Osnabrück. The colloquium aimed at strengthening algorithmic and methodological competencies, stipulating exchange between PhD candidates, and enhancing presentation and discussion skills. The program was thus set up to include presentations by PhD candidates, intensive discussions, which were chaired by the young scientists, as well as focused discussions in small working groups. An overview of bibliometrics was given by Ralf Bill, University of Rostock. The PhD colloquium was followed by a tutorial on mathematical programming, which was held by Jan-Henrik Haunert, University of Osnabrück. Lars Bernard, University of Dresden, completed the organization team.

As the result of an abstract-based review process, seven PhD students had been invited to give an in-depth (full) presentation of their work. Those PhD students presented their work in three sessions, which were dedicated to automated cartography, augmented reality, and algorithmic foundations of geoinformatics and photogrammetry. Participants without a full presentation had the opportunity to introduce themselves with a short talk.

Considering the very positive feedback from the participants, the colloquium, in the chosen format, was a full success. The Bohnenkamphaus in the botanical garden of the University of Osnabrück turned out to be the ideal location for the event, not least because it allowed for a relaxing walk to the historical

centre of Osnabrück, where the first day of the colloquium ended with conversations over pizzas and drinks.

The geoinformatics groups of DGK and DGPF aim to establish the PhD colloquium as an annual event. For 2016, the colloquium is planned to be held at the University of Bonn. Invitations will be forwarded via the subscription lists of DGPF and DGK.

Jan-Henrick Haunert, Osnabrück

Mitteilung der ISPRS

Neue ISPRS Kommissionsstruktur

Die ISPRS hat nach intensiven Diskussionen eine neue interne Struktur mit nunmehr fünf Kommissionen etabliert. Die neuen Kommissionen haben folgende Titel:

- Kommission I *„Sensorsysteme“*
- Kommission II *„Photogrammetrie“*
- Kommission III *„Fernerkundung“*
- Kommission IV *„Geoinformatik“*
- Kommission V *„Ausbildung und Öffentlichkeit“*

Beim ISPRS Kongress im Juli 2016 in Prag werden diese Kommissionen neu besetzt.

Weitere Informationen zu der Neustrukturierung der ISPRS Kommissionen sind unter http://www.isprs.org/news/announcements/150503-New_commission_structure.pdf zu finden.

Christian Heipke, Generalsekretär der ISPRS

In eigener Sache

Hansa-Luftbild-Preis: Neufassung der Statuten

Die Firma Hansa-Luftbild AG hat anlässlich ihres 50-jährigen Bestehens 1973 den Hansa-Luftbild-Preis gestiftet. Der Preis soll an Nachwuchswissenschaftlerinnen und Nachwuchswissenschaftler verliehen werden, die den besten Artikel eines Jahrgangs in der PFG veröffentlicht haben, vor allem in Hinblick auf praktische Anwendungen.

Die meisten Artikel der PFG haben heute mehrere Autoren, unter ihnen oft auch die das Thema betreuenden Professorinnen und Professoren. Nach den bisherigen Statuten waren derartige Artikel von einer Preisverleihung ausgeschlossen.

Die neuen Statuten fordern den Nachwuchswissenschaftler nur bei der Erstautorin oder dem Erstautor und erlauben so eine angemessene Berücksichtigung einer Vielzahl weiterer Artikel.

Der volle Wortlaut der Statuten ist auf der Homepage der DGPF verfügbar.

Wolfgang Kresse, Neubrandenburg

Veranstaltungskalender

2015

28. – 30. Oktober: **Joint International Geoinformation Conference 2015: 3DGeoInfo – GeoAdvances – ISPRS WGII/2 Workshop – Geomatic & Geospatial Technology** in **Kuala Lumpur**, Malaysia. www.geoinfo.utm.my/jointgeoinfo2015/

3. – 4. November: **Workshop 3D-Stadtmodelle** in **Bonn,** 3d-stadtmodelle.org

3. – 4. Dezember: **3D-NordOst 2015** in **Berlin**. 3d-NordOst.de

7. – 13. Dezember: **ICCV 2015 – International Conference for Computer Vision 2015** in **Santiago**, Chile. pamitc.org/iccv15/

9. – 11. Dezember: **MMT 2015: 9th International Symposium on Mobile Mapping Technology** in **Sydney**, Australien. mmt2015.org

2016

3. – 4. Februar: **Oldenburger 3D Tage** in **Oldenburg**. jade-hs.de/fachbereiche/bauwesen-und-geoinformation/geoinformation/oldenburger-3d-tage

10. – 15. Juli: **IGARSS 2016 – International Geoscience and Remote Sensing Symposium 2015** in **Peking**, China. igarss2016.org

12. – 19. Juli: **ISPRS Congress 2016** in **Prag**, Tschechien. www.isprs2016-prague.com

10. – 16. Oktober: **ECCV 2016 – European Conference on Computer Vision 2016** in **Amsterdam**, Niederlande. eccv2016.org

8. – 11. November: **ICPR 2016 – International Conference on Pattern Recognition 2016** in **Cancun**, Mexiko.

Weitere Konferenzen und Workshops finden sich beispielsweise unter:
isprs.org/calendar/Default.aspx
conferences.visionbib.com

Korporative Mitglieder

Firmen

AEROWEST GmbH
AICON 3D Systems GmbH
aphos Leipzig AG
ASTEC GEODATA GmbH
Bernhard Harzer Verlag GmbH
Black Bridge AG
Blom Deutschland GmbH
Brockmann Consult GmbH
bsf swissphoto GmbH
Büro Immekus
DB Netz AG
DELPHI IMM GmbH
Deutsches Bergbau-Museum
EFTAS Fernerkundung Technologietransfer GmbH
ESG Elektroniksystem- und Logistik-GmbH
Esri Deutschland GmbH
EUROPEAN SPACE IMAGING
Eurosense GmbH
Exelis Visual Information Solutions GmbH
fokus GmbH
GAF GmbH
GeoCart Herten GmbH
Geoinform. & Photogr. Engin. Dr. Kruck & Co. GbR
geoplana Ingenieurgesellschaft mbH
GEOSYSTEMS GmbH
GGS - Büro für Geotechnik, Geoinformatik, Service
Hansa Luftbild AG
Herbert Wichmann, VDE Verlag GmbH
IAGB mbH
IGI - Ingenieur-Gesellschaft für Interfaces mbH
ILV-Fernerkundungs GmbH
Infoterra GmbH
INVERS - Industrievermessung & Systeme
Leica Geosystems GmbH
Linsinger ZT GmbH
Luftbilddatenbank Dr. Carls GmbH
map/x/tek
Messbildstelle GmbH
Microsoft Photogrammetry
MILAN Geoservice GmbH
M.O.S.S. Computer Grafik Systeme GmbH
PHOENICS GmbH
PMS – Photo Mess Systeme AG
RIEGL Laser Measurement Systems GmbH
RWE Power AG, Geobasisdaten/Markscheidewesen
technet GmbH
Terra-Messflug GmbH
topometric GmbH
TRIGIS GmbH
Trimble Germany GmbH
trimetric 3D Service GmbH
Z/I Imaging Ltd.

Behörden

Bayerische Landesanstalt für Wald und Forstwirtschaft
Bundesamt für Kartographie und Geodäsie
Bundesmininisterium für Ernährung, Landwirtschaft und Verbraucherschutz
Hessisches LA für Bodenmanagement und Geoinformation
Innenministerium NRW, Gruppe Vermessungswesen
Institut für Umwelt- und Zukunftsforschung
LA für Geoinformation und Landentwicklung, BW
LA für Vermessung und Geoinformation, Bayern
LA für Vermessung und Geoinformation, Schleswig-Holstein
LB Geoinformation und Vermessung, Hamburg
LB für Küstenschutz, Nationalpark und Meeresschutz, SH
Landeshauptstadt Düsseldorf, Vermessungs- und Liegenschaftsamt
Landesvermessung und Geobasisinformation Niedersachsen
Märkischer Kreis, Vermessungs- und Katasteramt
Regierungspräsident Tübingen, Abt. 8 Forstdirektion
Regionalverband Ruhr
Staatsbetrieb Sachsenforst
Stadt Köln, Amt für Liegenschaften, Vermessung und Kataster
Stadt Wuppertal, Vermessung, Katasteramt und Geodaten
Thüringer LA für Vermessung und Geoinformation
Zentrum für Geoinformationswesen der Bundeswehr

Hochschulen

BTU Cottbus, Lehrstuhl für Vermessungskunde
FH Frankfurt a.M., FB 1, Studiengang Geoinformation
FH Mainz, Institut für Raumbezogene Informations- und Messtechnik
HCU HafenCity Universität Hamburg, Geomatik
HfT Stuttgart, Vermessung und Geoinformatik
HS Bochum, FB Vermessung und Geoinformatik
HS Karlsruhe, Fakultät für Geomatik
HTW Dresden, FB Vermessungswesen/Kartographie
Jade Hochschule, Institut für Angewandte Photogrammetrie und Geoinformatik
LUH Hannover, Institut für Kartographie und Geoinformatik
LUH Hannover, Institut für Photogrammetrie und Geoinformation
MLU Halle, FG Geofernerkundung
Rhein Ahr Campus, Anwendungszentrum für multimodale und luftgestützte Sensorik
Ruhr-Uni Bochum, Geographisches Institut
RWTH Aachen, Geodätisches Institut
TU Bergakademie Freiberg, Institut für Markscheidewesen und Geodäsie
TU Berlin, Computer Vision & Remote Sensing
TU Berlin, Institut für Geodäsie und Geoinformationstechnik
TU Braunschweig, Institut für Geodäsie und Photogr.
TU Clausthal, Institut für Geotechnik und Markscheidewesen
TU Darmstadt, Institut für Geodäsie, FG Fernerkundung und Bildanalyse
TU Dresden, Institut für Photogrammetrie und Fernerkundung
TU München, FG Photogrammetrie und Fernerkundung
TU München, Lehrstuhl für Geoinformatik
TU Wien, FG Photogrammetrie und Fernerkundung
Uni Bonn, Institut für Photogrammetrie
Uni Göttingen, Abt. Waldinventur und Fernerkundung
Uni Heidelberg, IWR Interdisziplinäres Zentrum für Wissenschaftliches Rechnen
Uni Kassel, FG Grünlandwissenschaften und Rohstoffe
Uni Kiel, Geographisches Institut
Uni Stuttgart, Institut für Photogrammetrie
Uni Trier, Institut für Umweltfernerkundung und Geoinformatik
Uni Würzburg, Geographisches Institut
Uni zu Köln, Geographisches Institut